Rapid Two-Dimensional One-Quantum and Two-Quantum Fluorescence Spectroscopy

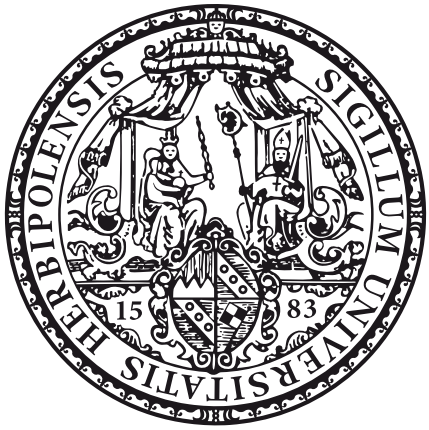

Dissertation zur Erlangung
des naturwissenschaftlichen Doktorgrades
der Julius-Maximilians-Universität Würzburg

vorgelegt von

Simon Draeger

aus Flensburg

Würzburg, 2019

Eingereicht bei der Fakultät für Chemie und Pharmazie am 09. August 2019

Gutachter der schriftlichen Arbeit
1. Gutachter: Prof. Dr. T. Brixner
2. Gutachter: Prof. Dr. I. Fischer

Prüfer des öffentlichen Promotionskolloquiums
1. Prüfer: Prof. Dr. T. Brixner
2. Prüfer: Prof. Dr. I. Fischer
3. Prüfer: Dr. F. Beuerle

Datum des Promotionskolloquiums: 06. Dezember 2019

List of Publications

Parts of this thesis have been published in the following references:

Reference [1]:

S. Draeger, S. Roeding, and T. Brixner,
Rapid-scan coherent 2D fluorescence spectroscopy,
Opt. Express **25**(4), 3259–3267 (2017).

Reference [2]:

S. Mueller, S. Draeger, X. Ma, M. Hensen, T. Kenneweg, W. Pfeiffer, and T. Brixner,
Fluorescence-Detected Two-Quantum and One-Quantum-Two-Quantum 2D Electronic Spectroscopy,
J. Phys. Chem. Lett. **9**, 1964–1969 (2018).

Reference [3]:

S. Mueller, S. Draeger, N. Klosterhalfen, and T. Brixner,
Fluorescence-Detected Two-Quantum and One-Quantum-Two-Quantum 2D Electronic Spectroscopy of Rhodamine 700,
EPJ Web Conf. **205**, 03012 (2019).

The publications listed above have partly been used in this dissertation. The following table itemizes where and to what extent the different sections of the publications have been reused. The sources of reproduced figures are additionally indicated at the end of the corresponding figure captions.

Publication	Usage	Dissertation
Ref. [1]		
p. 3	text adapted, modified and extended	p. 1
p. 4	text adapted, modified and extended	pp. 6–9
pp. 5–6	text reproduced and extended	pp. 21–23
pp. 7–9	text adapted and modified, reproduced and extended; figures reproduced	p. 19, pp. 39–43
Ref. [2]		
pp. 2–4	text adapted, modified and extended; figures adapted and modified	p. 46, pp. 53–56
Supporting Information	text reproduced and extended; figures adapted	pp. 47–53

Inhaltsverzeichnis

List of Publications I

1 Introduction 1

2 Ultrafast Spectroscopy 3
- 2.1 Nonlinear spectroscopy . . . 3
- 2.2 Coherent two-dimensional optical spectroscopy . . . 6
  - 2.2.1 Coherence-detected 2D spectroscopy . . . 6
  - 2.2.2 Population-based 2D spectroscopy . . . 8
- 2.3 Experimental techniques . . . 15
  - 2.3.1 Pulse generation . . . 15
  - 2.3.2 Pulse shaping methods . . . 16

3 Experimental implementation 21
- 3.1 Experimental setup . . . 21
- 3.2 Pulse shaper implementation . . . 23
- 3.3 Comparison of white-light generation methods . . . 25
- 3.4 Signal Detection . . . 27
- 3.5 Artifact sources and correction . . . 29
  - 3.5.1 Fourier-transformation artifact . . . 29
  - 3.5.2 Pulse-shaper artifact . . . 30
  - 3.5.3 Detector artifact . . . 32
- 3.6 Summary . . . 33

4 One-Quantum Two-Dimensional Spectroscopy 35
- 4.1 Data acquisition and analysis . . . 35
  - 4.1.1 Experimental parameter settings . . . 35
  - 4.1.2 Fluorescence signal . . . 36
  - 4.1.3 Raw time domain data . . . 37
  - 4.1.4 Phase-cycled 2D maps in time and frequency . . . 39
  - 4.1.5 2D absorptive spectra and time evolution . . . 39
- 4.2 Error evolution . . . 42
- 4.3 Summary . . . 43

5 Two-Quantum Two-Dimensional Spectroscopy 45
- 5.1 Experimental parameter settings . . . 45

5.2 Simulations 47
5.2.1 Influence of fluorescence quantum yield 47
5.2.2 Simulation parameters for modeling of experimental data . . . 50
5.2.3 Influence of excitation spectrum 52
5.3 Data analysis 53
5.4 Summary 55

6 Summary **57**

7 Zusammenfassung **59**

Bibliography **61**

Acknowledgements

1 Introduction

Light is life. The energy provided by the sun via electromagnetic radiation constitutes the foundation of life on earth. Photosynthetic organisms and the human vision are just two examples, where life has perfectly adapted to the spectrum of the sunlight.

In the last years, increasing awareness of global warming has led to an expanding need of alternative energy sources than fossil fuels, with photovoltaics being the most direct way to convert the energy provided by the sun. In order to use solar energy as efficiently as possible, it is extremely helpful to understand the energy-transport processes in nature. The underlying light-matter interactions and the induced chemical dynamics in photosynthesis and many other photoreactions happen on an ultrafast time scale, requiring an according time resolution. Femtosecond lasers provide the means to resolve these processes [4].

As a formal extension of pump-probe spectroscopy, coherent two-dimensional (2D) optical spectroscopy [5–8] has emerged as a powerful tool to reveal dynamic processes in various quantum systems [5, 7], for example delivering information about energy transport in light-harvesting systems [9]. Apart from light harvesting, the range of applications covers other biological phenomena [9–14], photochemical reactions [15], semiconducting materials [16, 17] or solvent effects on catalyst dynamics [18]. Originally developed for nuclear magnetic resonance techniques [19], optical coherent 2D experiments have been suggested [20, 21] and experimentally reported for nonlinear optics [22] as well as measurements of quantum dynamics with spectral ranges from the ultraviolet [23, 24] over the visible [25–27], the near-infrared [28] and the infrared [29], up to the THz regime [30].

Various nonlinear contributions contain information about the investigated quantum system like electronic couplings and wave-packet dynamics. There are two approaches to extract these contributions after interaction with a pulse sequence. Either an appropriate geometry is required to spatially separate the coherent system response in coherence-detected 2D spectroscopy [5], or the contribution-specific phases have to be encoded in the excitation-pulse sequence in population-detected 2D spectroscopy [31]. The observable in the latter case is an incoherent signal, from which the nonlinear contributions can be extracted via phase cycling.

Population-based 2D spectroscopy has been demonstrated on all states of matter utilizing fluorescence [32–37], photoelectrons [38–40], and ions [41] as incoherent observables. It has recently been suggested that the information content is even higher than in coherence-detected 2D spectroscopy, since processes can occur on a longer time scale than just the duration of the excitation-pulse sequence [42].

The retrieval of one-quantum (1Q) contributions in population-based 2D spectroscopy is well established [31–40], while two-quantum (2Q) 2D spectroscopy has so far only been carried out coherence-detected [17, 43, 44, 44–51].

The aim of this thesis is the realization of a pulse-shaper assisted all-collinear setup for fluorescence-detected 2D electronic spectroscopy. Shot-to-shot variation of pulses with 1 kHz repetition rate is supposed to keep the acquisition time to a minimum. By selecting an appropriate phase-cycling scheme, 1Q and 2Q nonlinear contributions shall be obtained in a single measurement.

Chapter 2 shall provide an overview over the theoretical concepts and experimental approaches that constitute the basis for this work. This includes a general description of nonlinear optical processes and how they can be revealed by coherent two-dimensional (2D) spectroscopy. Different approaches of coherent 2D spectroscopy in noncollinear and collinear geometry are reviewed and compared. The principles of phase cycling are presented which are indispensable for population-based spectroscopy. Furthermore, the utilized experimental techniques, including pulse generation and pulse shaping, are introduced.

In chapter 3 the implementation of the experimental techniques is described. The experimental setup is presented, with an emphasis on pulse generation and shaping as well as signal detection. An evaluation of pulse-generation techniques is given with respect to the requirements of the conducted experiments. We finally review possible artifact sources and show how to either avoid or correct them.

In chapter 4, we show the results of a 2D experiment on cresyl violet in ethanol as a proof of principle. All data-acquisition and analysis steps are presented in detail to provide a guideline for future experiments with this setup. Various nonlinear contributions are extracted during a single measurement, where shot-to-shot variation of excitation pulses is exploited for rapid data acquisition. The well-known rephasing and nonrephasing 1Q contributions are used to reproduce oscillatory behavior during the population time. We furthermore evaluate the error evolution with respect to the amount of averaging that is needed to obtain decent data, and by that give an estimation of the setup's potential concerning the acquisition speed.

In chapter 5, the setup is extended to broadband excitation. We obtain two types of 2Q coherence contributions of cresyl violet in a single measurement and show the first experimental data of the theoretically predicted 1Q-2Q contribution. The results are discussed and validated on the basis of simulations via the Lindblad quantum master equation. The simulations are used to evaluate the influence of the excitation spectrum on the obtained 2D data, to reveal the effect of Liouville pathway cancellation, and furthermore to determine the correlation energy of the doubly-excited state with a higher accuracy than with just the experiment.

The presented 2D fluorescence setup is evaluated in chapter 6 by providing a summary of this thesis' findings, as well as a perspective on possible future experiments.

2 Ultrafast Spectroscopy

The principles of ultrafast spectroscopy, ranging from the theoretical description of light-matter interaction to state-of-the-art experimental implementation, are summarized in this chapter. Section 2.1 will provide a basic description of nonlinear polarization and density matrix formalism. On that basis, a review of different approaches to coherent 2D spectroscopy is given in section 2.2, including the most commonly applied coherence-detected 2D spectroscopy in section 2.2.1 and the population-based method utilizing phase cycling in section 2.2.2. Since phase cycling is a key method to this work, detailed information about phase-cycling schemes for three- and four-pulse sequences will be provided alongside with Liouville-pathway selection via Feynman diagrams. Relevant experimental techniques, ranging from pulse generation (2.3.1) over pulse shaping (2.3.2) to resulting experimental opportunities like pulse compression, rotating-frame measurements and the economy of scan schems will be introduced in section 2.3.

2.1 Nonlinear spectroscopy

The following examination of the theoretical concepts has been adapted from textbooks [8, 21]. Upon light-matter interaction with an electric field E, a material polarization is induced which can be described by the perturbative power series

$$P(t') = \sum_{n}^{\infty} \epsilon_0 \left(\chi^{(n)} E^n(t')\right) = \epsilon_0 \left(\chi^{(1)} E(t') + \chi^{(2)} E^2(t') + \chi^{(3)} E^3(t') + ...\right) \qquad (2.1)$$

with vacuum permittivity ϵ_0 and the electric susceptibility χ of n-th order and assuming infinitesimal short electric fields for simplicity. The dependency of $P(t')$ on the wave vector $\mathbf{k}$ is omitted for brevity. Note that absolute times are denoted as t' because in two-dimensional spectroscopy t is reserved for the signal time or the second coherence time, respectively.

For weak fields, only the first-order polarization term $P^{(1)}(t') = \epsilon_0 \chi^{(1)} E(t')$ is accessible, yielding the linear absorption (imaginary part) and the refractive index (real part) of a material. Increasing the intensity of the incident light field, however, gives rise to higher-order nonlinear polarization terms $P^{(n)}(t')$ with $n \neq 1$. Ultrashort laser pulses provide the means to reach such intensities. Susceptibilities of an even order always equal zero for isotropic media, and thus the lowest nonlinear response

for isotropic media is given by $\chi^{(3)}$. Polarization upon light-matter interaction up to the third order plays a key role for for coherent 2D spectroscopy (section 2.3.1) as well as for ultrashort pulse generation (section 2.3.1).

Density matrix formalism

Apart from single-molecule experiments, nonlinear spectroscopy is performed on statistical ensembles of molecules, where each molecule of the ensemble has a different microscopic environment and therefore a different wave function. In order to account for this circumstance, the density matrix formalism is introduced, with the density matrix given by

$$\rho(t') = \sum_{k,l} p_{kl} \left|\psi_k(t')\right\rangle \left\langle\psi_l(t')\right| , \tag{2.2}$$

with p_{kl} (with $k = l$) being the probability of a molecule located in state $|\psi_k(t')\rangle$. For the total ensemble $\sum_{k,l} p_{kl} = \mathbf{Tr}\left[\rho(t')\right] = 1$, $k = l$ holds. The diagonal elements of a density matrix correspond to *populations*, and off-diagonal elements denote *coherences* [52, 53].

The time-dependent density matrix in Liouville-von Neumann equation is given by

$$\frac{\delta\rho(t')}{\delta t'} = -\frac{i}{\hbar}\left[H(t'), \rho(t')\right] = -\frac{i}{\hbar}\left[H_0, \rho(t')\right] - \frac{i}{\hbar}\left[H_I(t'), \rho(t')\right] \tag{2.3}$$

with the system Hamiltonian H_0, and the time-dependent interaction Hamiltonian $H_I(t')$. The time-dependent density matrix can be expanded in a perturbative power series analogously to the polarization via

$$\rho(t') = \sum_{n}^{\infty} \rho^{(n)}(t'), \tag{2.4}$$

where H_0 acts on $\rho^{(0)}$ assuming a thermal equilibrium, and H_I applies to $\rho^{(n)}$ with $n \neq 0$. The macroscopic observable of the n-th order perturbation $\rho^{(n)}(t')$ is the nonlinear polarization $P^{(n)}(t')$ after the last perturbation from an off-diagonal coherence of the density matrix, given by the expectation value of the dipole operator $\hat{\mu}$

$$P^{(n)}(t') = \mathbf{Tr}\left(\hat{\mu}\rho^{(n)}(t')\right) \tag{2.5}$$

The time dependent polarization of n-th order is a convolution of an n-th-order response function $S^{(n)}$ with n light fields E

$$P^{(n)}(t') = \int_{-\infty}^{\infty} dt_n \int_{-\infty}^{\infty} dt_{n-1} ... \int_{-\infty}^{\infty} dt_1 S^{(n)}(t_n, t_{n-1}, ..., t_1) \\ E(t' - t_n)E(t' - t_n - t_{n-1})...E(t' - t_n - t_{n-1} ... - t_1). \tag{2.6}$$

where t_i are the times at which a light-matter interaction occurs. In contrast to eq. (2.1), it is accounted for the non-zero duration of the electric fields.

In coherence-detected 2D experiments, the third-order polarization is probed. Accordingly, three successive interactions with electric fields E at t_i induce the third-order polarization

$$P^{(3)}(t') = \int dt_3 \int dt_2 \int dt_1 S^{(3)}(t_1, t_2, t_3) \\ E(t' - t_3)E(t' - t_3 - t_2)E(t' - t_3 - t_2 - t_1), \tag{2.7}$$

corresponding to the third-order perturbation term of the density matrix.

The polarized system can emit a coherent signal as an electric field $E_S \propto P^{(3)}$. The manifold of response functions S can be obtained by bookkeeping of all possible pathways through the density matrix, called *Liouville pathways*. Double-sided *Feynman diagrams* can be used to describe these pathways in an illustrative manner. The principles of Feynman diagrams and relevant pathways for this thesis will be discussed in section 2.2.2.

Adding a further light-matter interaction leads to a *fourth-order population*, which is of interest in the *population-based* approach of 2D spectroscopy. Instead of a coherent field, the observable is an incoherent signal like fluorescence, ions or photoelectrons, while the information content is analogous. For clarity, the fourth-order population will be written as $p^{(4)}$, corresponding to a fourth-order perturbation of the density matrix $\rho^{(4)}$:

$$\begin{aligned} p^{(4)}(t') \equiv & \rho^{(4)}(t') \\ = & \int dt_4 \int dt_3 \int dt_2 \int dt_1 Q^{(4)}(t_1, t_2, t_3, t_4) \\ & E(t' - t_4)E(t' - t_4 - t_3)E(t' - t_4 - t_3 - t_2)E(t' - t_4 - t_3 - t_2 - t_1). \end{aligned} \tag{2.8}$$

where the response function is written as Q for the sake of distinguishability from the response function S in eq. (2.7).

2.2 Coherent two-dimensional optical spectroscopy

An intuitive approach of measuring the time evolution of a quantum system is constituted by pump-probe spectroscopy. A pump pulse excites the system and a second pulse probes the system evolution after a population time T. This method has been extensively used on a vast variety of chemical systems, delivering insights in chemical dynamics with a femtosecond time resolution.

As in pump-probe spectroscopy, coherent two-dimensional (2D) spectroscopy can reveal the evolution of a chemical system. Due to the equivalence between time and frequency via Fourier transform, spectral information can be obtained with time-dependent measurements. To that purpose, two pump pulses are applied and delayed incrementally. Only system responses resulting from third-order polarization (or fourth-order population) shall be considered, since most reported 2D experiments as well as this thesis investigate such signals. Higher-order polarization can be used to investigate, e. g., exciton-exciton interactions [54, 55]. The higher the order of the induced polarization, the larger the amount of possible pathways becomes.

There is a variety of methods to perform 2D spectroscopy. This section shall provide an overview over existing approaches, comparing the phase-matching approach in a noncollinear geometry with the population-based approach, where coherent system information is obtained via an incoherent signal and extracted via phase cycling. Since this work follows the population-based approach, phase-cycling theory will be examined in more detail in order to provide an understanding for the experiments that will be discussed in chapters 3, 4 and 5.

2.2.1 Coherence-detected 2D spectroscopy

Many 2D experiments employ three excitation pulses, and the coherently emitted nonlinear four-wave-mixing signal is measured in amplitude and phase. Extracting the desired signal component of a certain nonlinear order (such as the photon-echo contribution) is generally achieved in the noncollinear box geometry under a suitable phase-matching condition, i.e., choosing an appropriate excitation and detection geometry [5]. By employing a noncollinear geometry, signal ambiguities are excluded by spatially separating the desired nonlinear signal from the excitation pulses as well as from other nonlinear signal components.

The excitation scheme of a quantum system with electronic states $|i\rangle$ and $|j\rangle$ is as follows. Each pump pulse interacts once with the system, where the first pulse converts the system into a coherent state $|j\rangle\langle i|$ with $i \neq j$. During the coherence time τ, the induced coherence decays within tens to hundreds of femtoseconds. The second pump pulse creates a population $|j\rangle\langle j|$ that can undergo relaxation during the population time T via internal conversion (IC), intramolecular vibrational energy distribution (IVR), intersystem crossing (ISC), conical intersections (CI) or fluorescence. The third pulse probes the system by again creating a coherence, which can

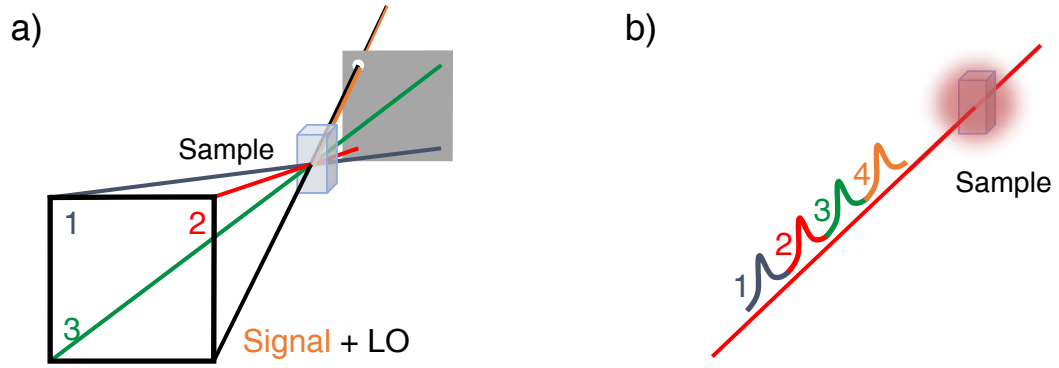

Figure 2.1: Schematic illustration of approaches to 2D spectroscopy. a) In the coherence-detected approach the excitation pulses $1, 2, 3$ are non-collinearly focused on the sample and the coherent signal from third-order polarization is extracted via heterodyne detection with a local oscillator (LO). b) In the population-based approach, a collinear pulse sequence excites the sample and induces a fluorescence signal of a fourth-order population. The coherent information is encoded in the phases of the excitation-pulse sequence and the signal is extracted via phase cycling (not shown).

emit a measurable electric field E_S after the signal time t. A fourth pulse acts as a local oscillator and is used for heterodyne detection of the coherent field E_S on a spectrometer, resulting in a frequency axis ω_t. Figure 2.1 a) illustrates schematically the noncollinear box geometry.

For each population time, Fourier transform along the coherence time spans a second axis along ω_τ, corresponding to the excitation process and correlating it with the emission spectrum along ω_t. The information content of a 2D spectrum depends on the obtained nonlinear contribution. The rephasing and nonrephasing contribution yield together the absorptive spectrum, which is analogous to signals acquired in pump-probe spectroscopy. For example, the rephasing photon echo is emitted in direction $\mathbf{k}_\mathrm{S} = -\mathbf{k}_1 + \mathbf{k}_2 + \mathbf{k}_3$, where $\mathbf{k}_i, i = 1, 2, 3$, are the wavevectors of the three excitation pulses and $\mathbf{k}_\mathrm{S}$ is the wavevector of the coherent signal.

From these 2D maps, coupling between states can be revealed via off-diagonal cross peaks. The investigation of coupling between states can, e. g., be used for the revelation of coherent energy transfer pathways in biomolecules [56]. The diagonal peaks deliver information about homogeneous and inhomogeneous line broadening. The homogeneous broadening effects the peak width perpendicular to the diagonal, and is caused by population relaxation and phase randomization due to the ensemble averaging effect. Because each molecule encounters a different microscopic environment, the peak width is also broadened along the diagonal, called inhomogeneous

broadening. Note, that line shapes are influenced not only by the molecular response, but also by the excitation pulses. A detailed analysis of finite-pulse effects is given in [57] and [58] and discussed in chapter 5.

Two-quantum (2Q) coherences can be measured to determine the correlation energy between excited states. In that case, the first two interactions transfer the system into a coherence between the ground and a doubly excited state. 2Q 2D spectroscopy can be used to determine an energy shift Δ, of which is stated that it may be consulted to quantify the theoretically predicted electron correlation energy in many-electron systems [59].

In general, 2D experiments in boxcar geometry require meticulous adjustment and effort to grant phase stability, and to achieve spatial and temporal pulse overlap. Furthermore, due to uncertainties in pulse overlap at $\tau = 0$, a phasing procedure is indispensable for correct data representation [60]. Even though it is possible to passively stabilize the phases of the noncollinear pulses [27], it is desirable to reduce the alignment effort to a minimum, especially in laboratories with many different experiments and frequent laser-path changes.

2.2.2 Population-based 2D spectroscopy

Instead of measuring an emitted coherent signal one can also utilize 2D action-based spectroscopy [31, 32, 38, 39, 61, 62]. For that purpose a fourth pulse is added to the excitation sequence, leaving the quantum system in a final population state, rather than a coherence. This final-state population can be probed, for example, via fluorescence [31,32,61], electron current [38,39], or ions [41]. The additional coherence time t has to be Fourier transformed analogously to τ to span the second frequency axis. The coherent information is encoded in the train of excitation pulses and their phase relations [62]. Fluorescence 2D spectroscopy in the visible regime has been demonstrated in the gas phase [31] as well as in liquids [35] and matrices [33]. Performing coherent 2D experiments is challenging with respect to phase and intensity stability of the laser as well as spatial and temporal alignment of the excitation pulses. Any drifts or fluctuations might lead to experimental artifacts, especially considering the phase-sensitive nature of the spectroscopy method and its Fourier evaluation process. Additionally, the high-intensity light fields that need to be applied for obtaining nonlinear signals may lead to decomposition of the investigated quantum systems, via, e. g., photochemical reactions resulting in permanent bleaching. Further, when one wants to make comparative studies of a series of quantum systems via 2D spectroscopy, one needs to ensure that the experimental conditions remain constant. All of these challenges make it desirable to keep the acquisition time down to a minimum. In collinear geometry, schematically depicted in fig. 2.1 b), the different contributions of the system response cannot be distinguished spatially, and anyway with incoherent fluorescence detection no phase-matching condition exists. Accordingly, a different approach for extraction of nonlinear contributions has to be applied.

One possibility is given by the *phase modulation* approach [32]. There, the incident pulse is split into four beam paths, such that three of the resulting pulses can be separately delayed via mechanical stages. Four acousto-optic modulators are used to continuously sweep the carrier-envelope phase of each beam path with a unique frequency before recollinearizing the pulses in front of the sample. Accordingly, each combination of laser shots exposes an amplitude modulation due to the differing phase combinations which can be disentangled via lock-in detectors. This approach thus requires a rather sophisticated setup and time-consuming adjustment.

Alternatively, *phase cycling* can be used to obtain all nonlinear contributions, such as rephasing, nonrephasing and two-quantum coherences [62]. For this purpose, a pulse shaper (2.3.2) is used to apply prescribed phases to each of the excitation pulses, and the desired signal is then obtained as a suitable linear combination of fluorescence intensities. In order to measure a fluorescence signal, the system has to be in an excited-state population after the fourth interaction.

Liouville pathway selection

The considerations in this section follow the description of Mukamel's textbook [21]. Figure 2.2 illustrates the Liouville pathways of the rephasing (R, a), nonrephasing (NR, b), 2Q (c), and 1Q-2Q (d) contributions in an electronic three-level system with states $|g\rangle$, $|e\rangle$ and $|f\rangle$ via double-sided Feynman diagrams [63–65], with the subsequent fluorescence signal not shown.

The time axis t' in Feynman diagrams is running from bottom to top. Arrows indicate a perturbation of the density matrix, with the direction representing the sign of the pulse phase ϕ, or the wave vector $\mathbf{k}$ in noncollinear geometry, respectively. An arrow pointing left denotes a negative sign, while a right-pointed arrow represents a positive sign. When pointing towards the diagram they represent an excitation and a deexcitation when pointing away. The resulting overall sign of the signal contribution in the real-valued spectrum is given by $(-1)^{-n}$, with n being the number of interactions from the right side.

Coherences between neighbored electronic states, e. g., between ground and singly excited state or between singly and doubly excited state are considered as 1Q coherences. Nonlinear contributions that contain only 1Q coherences can be rephasing (photon echo) or nonrephasing [8], and accordingly, experiments that probe these can be regarded as 1Q 2D spectroscopy. If a 2Q coherence is part of the pathway, one may refer to this as 2Q 2D spectroscopy. A 2Q coherence describes a coherent superposition of the ground state $|g\rangle$ and the doubly excited state $|f\rangle$ generated via a two-photon process.

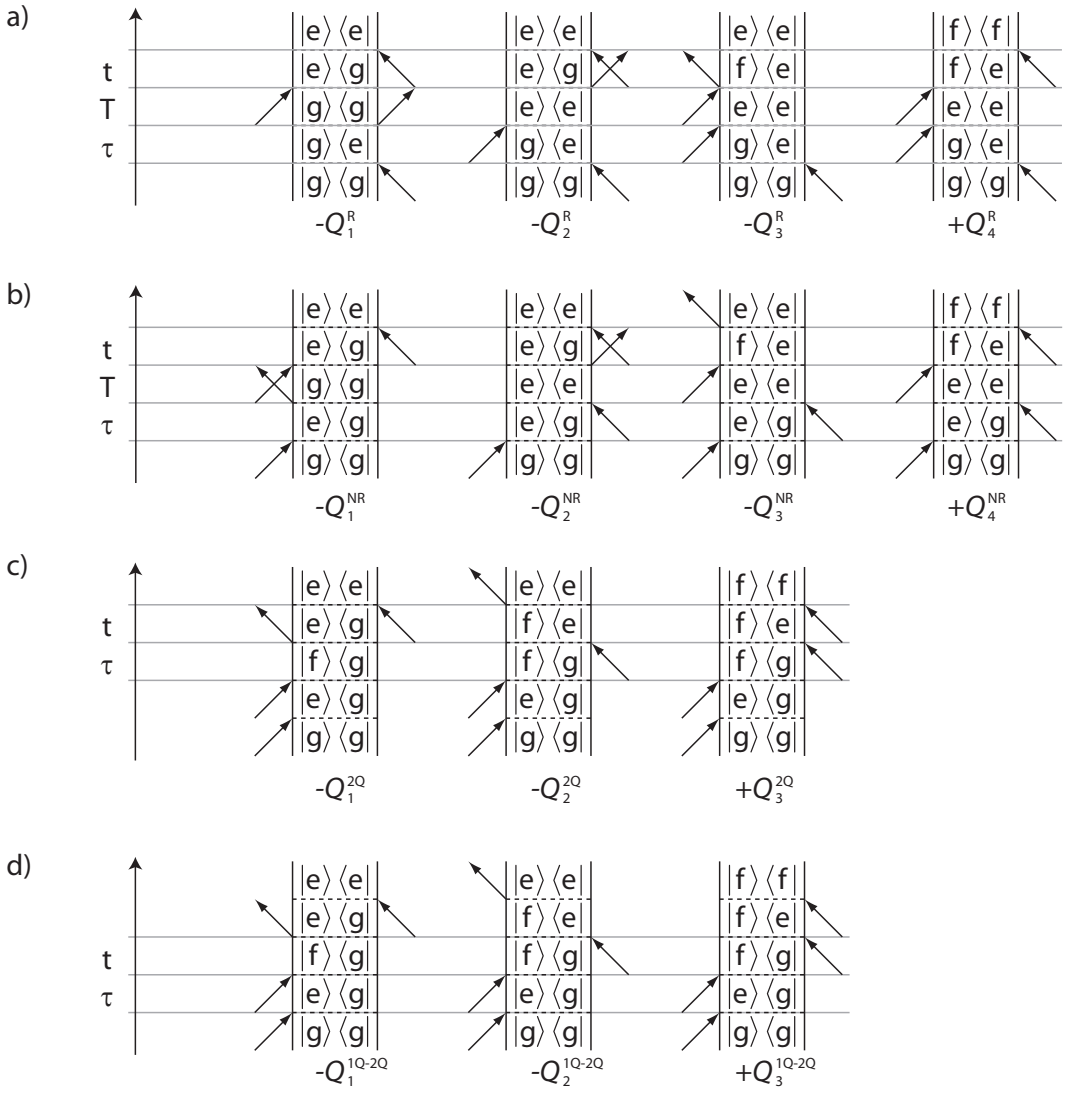

Figure 2.2: Liouville pathways of extractable nonlinear contributions in a three-level system in population based 2D spectroscopy. Rephasing (a), nonrephasing (b), 2Q-1Q (c), and 1Q-2Q (d). a) and b) describe the pathways in a four-pulse sequence, when all 4 interactions occur at specific times t_i with $i = 1, 2, 3, 4$, $\tau = t_2 - t_1$, $T = t_3 - t_2$, and $t = t_4 - t_3$. c) and d) refer to the pathways in a three-pulse sequence, where two interactions are at the same time $t_1 = t_2$ (c) and $t_3 = t_4$ (d), respectively. The pathway on the right in each row contributes with a positive sign, while all other pathways contribute with a negative sign. The subsequent fluorescence signal is omitted.

The contribution-dependent fourth-order population from eq. (2.8) for the nonlinear contribution convoluted with the incident electric field can be written as

$$p_{\mathrm{R}}^{(4)}(t') \propto Q^{\mathrm{R}}(\tau, T, t, t') e^{i\gamma_0\omega_0(t-T-\tau)} e^{i(-\phi_1+\phi_2+\phi_3-\phi_4)}, \tag{2.9}$$

$$p_{\mathrm{NR}}^{(4)}(t') \propto Q^{\mathrm{NR}}(\tau, T, t, t') e^{i\gamma_0\omega_0(t-T-\tau)} e^{i(+\phi_1-\phi_2+\phi_3-\phi_4)}, \tag{2.10}$$

$$p_{\mathrm{2Q}}^{(4)}(t') \propto Q^{\mathrm{2Q}}(\tau, t, t') e^{i\gamma_0\omega_0(t-T-\tau)} e^{i(+2\phi_1-\phi_2-\phi_3)}, \tag{2.11}$$

$$p_{\mathrm{1Q\text{-}2Q}}^{(4)}(t') \propto Q^{\mathrm{1Q\text{-}2Q}}(\tau, t, t') e^{i\gamma_0\omega_0(t-T-\tau)} e^{i(+\phi_1+\phi_2-2\phi_3)}, \tag{2.12}$$

where the signs of the phases ϕ_i correspond to phase coefficients α, β, γ (and δ), indicating if the interaction with the density matrix is from the left or the right side. The wave vector dependency $e^{i(\alpha\mathbf{k}_1+\beta\mathbf{k}_2+\gamma\mathbf{k}_3+\delta\mathbf{k}_4)\cdot\mathbf{r}}$ for a four-pulse sequence and $e^{i(\alpha\mathbf{k}_1+\beta\mathbf{k}_2+\gamma\mathbf{k}_3)\cdot\mathbf{r}}$ for a three-pulse sequence is neglected due to the collinearity of the approach. The parameter γ_0 is a frequency scaling factor that is implemented in pulse-shaper-based 2D spectroscopy to realize measurements in the rotating frame ($\gamma_0 = 0$) or the laboratory frame ($\gamma_0 = 1$) or an intermediate regime ($0 < \gamma_0 < 1$). The rotating-frame environment will be discussed later in section 2.3.2.

The nonlinear response functions Q^{NL} for each contribution contain terms Q_i^{NL}, the label i of which corresponds to the Liouville pathways shown in fig. 2.2. The pathways for a specific contribution are indistinguishable. It is apparent that only pathways ending up in the doubly excited state $|f\rangle$ exhibit an even amount of interactions from the right side, and thus contribute to the overall real-valued signals with a positive sign. Hence, the sign of the real-valued 2D spectra is expected to be strongly negative.

Recapitulating Kasha's rule [66], one may also conclude that these signal contributions might be not detectable at all, because a direct fluorescence from $|f\rangle$ is improbable for most molecules. In order to contribute to the respective measured fluorescence signal, there has to be considerable nonradiative relaxation from $|f\rangle$ to $|e\rangle$. If nonradiative deactivation pathways to the ground state exist, the contribution may be noticably less than unity [33, 34, 40]. An approach to estimate the contribution ratio will be presented in chapter 5. It is furthermore noteworthy that these right pathways Q_i^{NL} (with $i = 4$ for $\mathrm{NL} = \mathrm{R}, \mathrm{NR}$ and $i = 3$ for $\mathrm{NL} = \mathrm{2Q}, \mathrm{1Q\text{-}2Q}$) exclusively contribute in the population-based approach, because they are only distinguishable from pathways Q_{i-1}^{NL} by the fourth perturbation which is not present in the coherence-detected approach.

The same principle applies for the 1Q-2Q contribution, which is solely obtainable via population-based 2D spectroscopy. In this additional contribution, there are less coherence combinations involved, and thus the 1Q-2Q 2D spectra should be less congested than 2Q 2D spectra [62].

Since in Q^{2Q} and $Q^{\mathrm{1Q\text{-}2Q}}$ there are three instead of two pathways involved, identical 1Q transition frequencies will not lead to a cancellation of the overall signal as it would be the case with coherent detection [59]. The same holds for the 1Q-2Q contribution.

Nevertheless, pathways Q_2^{2Q} and Q_3^{2Q} (and also $Q_2^{1Q\text{-}2Q}$ and $Q_3^{1Q\text{-}2Q}$) may cancel each other out if their contribution strengths are equal.

As written above, 2Q 2D spectroscopy can be utilized to determine the correlation energy Δ. A detailed analysis of population-based 2Q and 1Q 2D spectroscopy on the example of cresyl violet will be provided in chapter 5.

Note that all Q^{NL} terms as well as terms of other orders contribute to the total fluorescence signal, with the desired nonlinear contributions making up only a small portion. In that sense, the method is not background-free and requires a high dynamic detector range. In order to unambiguously extract any desired nonlinear contribution, an appropriate phase-cycling scheme is required, which depends on the amount of pulses in the excitation-pulse sequence.

Four-pulse sequence

The phase-cycling procedure follows the description of Tan [62]. The most general approach to obtain information about the fourth-order population is given when applying a four-pulse sequence. In this case, every perturbation of the density matrix is induced by a single pulse, with each pulse considered separately. The delays between the pulses are regarded as coherence time $\tau = t_2 - t_1$, population time $T = t_3 - t_2$ and signal time $t = t_4 - t_3$. Incorporating the population time allows to observe the transient behavior of the investigated molecules.

Equations (2.9–2.12) can be generalized as

$$p_{\mathrm{NL}}^{(4)}(t') = \propto Q^{\mathrm{NL}}(\tau, T, t, t') e^{i\gamma_0\omega_0(t-T-\tau)} e^{i(\alpha\phi_1+\beta\phi_2+\gamma\phi_3+\delta\phi_4)}, \tag{2.13}$$

with phase coefficients α, β, γ, δ.

The sum of the phase coefficients is required to be $\alpha + \beta + \gamma + \delta = 0$ since only populations contribute to the fluorescence signal. As an additional condition, the sum of their absolute values has to be $|\alpha| + |\beta| + |\gamma| + |\delta| \leq 4$ to only account for fourth- or lower order populations.

The contribution-specific fourth-order population may be represented with its phase-coefficient dependency via

$$\tilde{p}^{(4)}(\tau, T, t, \alpha, \beta, \gamma, \delta) = Q^{\mathrm{NL}}(\tau, T, t, t_4) e^{i\gamma_0\omega_0(t-T-\tau)}, \tag{2.14}$$

at time t_4, i. e. directly after the fourth interaction.

The total delay- and phase-dependent population including all nonlinear contributions is given by the sum over all phase coefficients

$$p^{(4)}(\tau, T, t, \phi_1, \phi_2, \phi_3, \phi_4) = \sum_{\alpha,\beta,\gamma,\delta} \tilde{p}^{(4)}(\tau, T, t, \alpha, \beta, \gamma, \delta) e^{i(\alpha\phi_1+\beta\phi_2+\gamma\phi_3+\delta\phi_4)}, \tag{2.15}$$

at time t_4, i. e. directly after the fourth interaction.

Considering that the phases are not independent of each other, this can be further simplified by referencing all phases ϕ_i to the first pulse ϕ_1

$$p^{(4)}(\tau, T, t, \Delta\phi_{21}, \Delta\phi_{31}, \Delta\phi_{41}) = \sum_{\beta,\gamma,\delta} \tilde{p}^{(4)}(\tau, T, t, \beta, \gamma, \delta) e^{i(\Delta\phi_{21}, \Delta\phi_{31}, \Delta\phi_{41})}, \tag{2.16}$$

with $\Delta\phi_{21} = \phi_2 - \phi_1$, $\Delta\phi_{31} = \phi_3 - \phi_1$, and $\Delta\phi_{41} = \phi_4 - \phi_1$.

In order to extract a specific nonlinear contributions via the phase coefficients, eq. (2.16) has to be Fourier transformed. Given that experimentally it is not possible to sample continuously, a discrete Fourier transform is necessary

$$\tilde{p}^{(4)}(\beta, \gamma, \delta) = \frac{1}{LMN} \sum_{n=0}^{N-1} \sum_{m=0}^{M-1} \sum_{l=0}^{L-1} p(\tau, T, t, l\Delta\phi_{21}, m\Delta\phi_{31}, n\Delta\phi_{41}) \\ e^{-il\beta\Delta\phi_{21}} e^{-im\gamma\Delta\phi_{31}} e^{-in\delta\Delta\phi_{41}}, \tag{2.17}$$

with $p(\tau, T, t, l\Delta\phi_{21}, m\Delta\phi_{31}, n\Delta\phi_{41})$ being the measured fluorescence signals, and L, M and N the number of sampling points, resulting in a $1 \times L \times M \times N$ measurement scheme.

A sampling resolution of $L = M = N = 3$ is sufficient to exclusively isolate the rephasing Q^{R} with $\beta = +1$, $\gamma = +1$, $\delta = -1$ and the nonrephasing Q^{NR} contribution with $\beta = -1$, $\gamma = +1$, $\delta = -1$, corresponding to coherently-detected 1Q 2D spectroscopy.

In principle it is possible to also extract 2Q and 1Q-2Q contributions with a four-pulse sequence. In the case of Q^{2Q}, the phase coefficients should be $\beta = 0$, $\gamma = -1$, $\delta = -1$. With a 27-fold phase-cycling scheme this contribution is not unambiguously extractable. When applying the 2Q phase coefficients, also signals with phase coefficents $\beta = 0$, $\gamma = +2$, $\delta = -1$ and $\beta = +1$, $\gamma = +1$, $\delta = -1$ contribute for $T = 0$. In order to exclusively extract the 2Q and 1Q-2Q contribution with a four-pulse sequence, a $1 \times 4 \times 4 \times 4$ scheme would be required, with the drawback of a huge increase in acquisition time.

Three-pulse sequence

In order to perform 2Q 2D spectroscopy, we employ a three-pulse sequence in this work. By definition, two interactions with the density matrix occur with one of the three pulses while the other two pulses interact once, resulting in the conditions $\alpha + \beta + \gamma = 0$ and $|\alpha| + |\beta| + |\gamma| \leq 4$.

Analogously to eq. (2.17), the desired nonlinear contribution can be extracted via

$$\tilde{p}^{(4)}(\beta,\gamma) = \frac{1}{LM}\sum_{m=0}^{M-1}\sum_{l=0}^{L-1} p(\tau,T,t,l\Delta\phi_{21},m\Delta\phi_{31}) \\ e^{-il\beta\Delta\phi_{21}}e^{-im\gamma\Delta\phi_{31}}. \tag{2.18}$$

With a three-pulse sequence and 16-fold phase cycling it is possible to unambiguously extract the rephasing contribution as well as the 2Q and 1Q-2Q contributions. The nonrephasing contribution is superimposed by contributions from second-order density-matrix perturbation terms which are also encoded when applying the factors $\alpha = 1$, $\beta = 0$ and $\gamma = -1$. It is therefore more appropriate to regard this contribution as a *reverse transient grating*.

2.3 Experimental techniques

This section is supposed to introduce the state-of-the-art experimental techniques that are utilized in this work, namely pulse generation with various white-light generation methods (2.3.1), pulse-shaping techniques and experimental benefits deriving from these, and pulse compression methods (2.3.2). The employment of the respective techniques in this work is further discussed later in chapter 3 and complemented with findings concerning their applicability for the presented experiments.

2.3.1 Pulse generation

Given a laser source with a specific fundamental wavelength, e. g., 800 nm as in the current work, there is a variety of possibilities to create white-light pulses from these input pulses. The two applied methods for white-light generation will be briefly introduced in the following. Relevant nonlinear optical effects are *second-harmonic generation* (SHG), *self-phase modulation* (SPM) and *optical parametric amplification* (OPA).

The SHG process is a $\chi^{(2)}$-process, requiring a birefringent crystal in order to survive destructive interference of the resulting radiation as would be the case in an isotropic medium. An intense pulse with a frequency ω_p induces a second-order polarization $P^{(2)}$ in a birefringent crystal. The refractive index of the resulting field with a frequency $2\omega_p$ differs from the the refractive index of the incident frequency. With the right crystal angle, i. e., correct phase-matching conditions, frequency-doubled pulses with a considerable intensity can be achieved.

SPM as a $\chi^{(3)}$-process can be induced in any medium via interaction with intense light. It relies on the optical Kerr effect [67, 68], according to which the refractive index of a material is intensity-dependent for high intensities. The effect of SPM is the creation of lower and higher frequencies that are symmetric to the initial center frequency ω_p, which can be exploited for broadband spectrum generation.

Noncollinear optical parametric amplification

Noncollinear optical parametric amplification (NOPA) is a standard method to generate tunable pulses over a broad range covering the visible and the near infrared (NIR) [69–71] and is indeed used in most 2D electronic spectroscopy setups [72].

For parts of this work (experiment in chapter 4), we employ a commercial two-stage noncollinear optical parametric amplifier (TOPAS, Light Conversion), the working principle of which shall be briefly explained. A detailed description is provided in the TOPAS user manual [73].

The TOPAS uses a combination of SHG, SPM and OPA to generate pulses in the visible range from an 800 nm input beam. The input beam is split with a ratio of $\approx 49:1$. The weak part is used to generate a supercontinuum via SPM in a sapphire

plate, while the major part is frequency-doubled in a β-barium borate (BBO) crystal via SHG. For the OPA process, the weak beam (seed) is overlapped with the intense frequency-doubled beam (pump) in a BBO crystal. This process is done twice in order to provide an intense and stable output. Varying the spatio-temporal overlap via delay stages and the BBO crystal angle adjusts the phase-matching conditions for a certain spectrum and thus enables tunability from $500 - 750$ nm [73].

Filamentation

Briefly, filamentation via SPM in a *hollow-core fiber* (HCF) filled with a noble gas can be used to generate a supercontinuum with a spectral broadness that can range over more than an octave. An advantage apart from the superior broadness is a clean and symmetric Gaussian beam profile, as well as a good compressibility of the pulses via chirped mirrors. This is especially useful for the presented pulse-shaper assisted 2D spectroscopy. Since in this case the probe pulse is a copy of the excitation pulses, both the pump and the probe pulses are limited by the primary white-light source and hence, increasing the spectral broadness effects both resulting frequency axes. The white-light generation via HCF in this work follows the description in [74].

2.3.2 Pulse shaping methods

The control of phase and amplitude of femtosecond pulses is indispensable for ultrafast spectroscopy, for mere pulse characterization and compression as well as for sophisticated arbitrary pulse-sequence generation. This section shall provide basic information about the phase influence on pulse shapes and review the working principles of the pulse-shaping methods employed in this work, ranging from passive shaping via prism and grism compression to active shaping via acousto-optical modulation.

Electric field and phase influence

A linearly polarized time-dependent electric field $E(t)$ can be described by [75]

$$E(t) = A(t)\cos(\Phi(t)), \tag{2.19}$$

with the envelope function $A(t)$ and the total phase

$$\Phi(t) = \omega_0 t + \phi(t). \tag{2.20}$$

The total phase contains the center frequency ω_0 and the time-dependent phase $\phi(t)$ which is given by the Taylor series

$$\phi(t) = \sum_{n=0}^{\infty} \frac{\phi_n}{n!} t^n = \phi_0 + \phi_1 \frac{t}{1!} + \phi_2 \frac{t^2}{2!} + \phi_3 \frac{t^3}{3!} + ..., \tag{2.21}$$

with phase coefficients $\phi_n = \frac{\partial^n \phi(t)}{\partial t^n}$. The first coefficient ϕ_0 describes the *carrier-envelope phase*, which is the phase of the intensity envelope with respect to the carrier frequency. If the phase terms ϕ_n with $n \geq 2$ are unequal zero, the pulse is broadened in time, resulting in an excess of the *bandwidth limit*.

The bandwidth limit $\tau_G \Delta\omega = 4 \ln 2$ describes the relationship between the shortest possible Gaussian pulse duration τ_G and the spectral *full width at half maximum* (FWHM) $\Delta\omega$.

In order to experimentally manipulate the phase coefficients of a laser pulse, the phase has to be regarded in the frequency domain as

$$\phi(\omega) = \sum_{m=0}^{\infty} \frac{\phi_m(\omega_0)}{m!} (\Delta\omega)^m = \phi_0 + \frac{1}{1!}\phi_1(\Delta\omega) + \frac{1}{2!}\phi_2(\Delta\omega)^2 + \frac{1}{3!}\phi_3(\Delta\omega)^3 + ..., \tag{2.22}$$

with $\phi_m = \frac{\partial^m \phi(\omega)}{\partial \omega^m}$, and $\Delta\omega = \omega - \omega_0$.

The first-order phase term, or *group delay* (GD), causes an equal shifting of all spectral components in the time domain. The second-order phase term is called *group-delay dispersion* (GDD) and causes a *chirp* which stretches the pulse in the time domain. Pre or post pulses are introduced by the *third-order dispersion* (TOD). Higher-order phase terms further stretch the pulses or introduce additional pulses. Since the speed of light in matter is different for each frequency component, a transmission through transparent materials always introduces a frequency-dependent phase which lengthens the pulse duration.

In ultrafast spectroscopy, however, short pulses are desirable for the sake of time resolution, and compression to the near-bandwidth limit is a condition for that. In the following, means of phase adjustment are introduced that are relevant for this work.

Static compression

For a given setup, the beam path leads through a known and constant amount of material, e. g. lenses, pulse-shaper crystal, or the sample capillary. In order to provide near-bandwidth limited pulses at the sample position, one can use passive pulse shaping methods for adjustment. The employed compression methods shall be shortly introduced.

The introduction of a negative GDD can be performed with a *single-prism compressor* [76]. In this work, the single-prism compressor is used to precompensate for the phase that is introduced by the Dazzler crystal. Apart from an input and

output mirrorm it consists of a prism, a retroreflector and a roof mirror. The beam passes the prism four times, where the first run introduces an angular dispersion, the second collimates the spectral parts and the third and fourth run correct the spatial and angular dispersion. The introduced phase can be adjusted by the prism angle and the distance between prism and retroreflector.

A *dual grism compressor* has a similar working principle but consists of two prisms that are equipped with a grating on the outside and a roof mirror. The beam passes the grisms twice, which is analogous to a fourfold passing through a single prism. The combination of prisms and grating enables to introduce TOD in addition to GDD. The amount of phase correction can be adjusted by varying the distance between the grisms, their offset of each other perpendicular to the beam and the incident angle. An elaborate description of the adjustment procedure can be found in the user manual of the utilized commercial device [77].

Collinear frequency-resolved optical gating

The pulses can be further compressed and characterized by *frequency-resolved optical gating* (FROG) [78]. In order to temporally resolve an event, a shorter event is needed. In the case of ultrashort pulses, they represent the shortest event available and are therefore used to resolve themselves, acting as gate pulses. In order to do so, two pulses are focused on a BBO crystal and delayed with respect to each other. In this work, collinear pulse-trains are used and hence collinear FROG (cFROG) is applied [79]. The delay- and frequency-dependent SHG signal is measured with a spectrometer, resulting in a two-dimensional FROG trace

$$I_{cFROG}^{SHG}(\omega,\tau) = \left| \int_{-\infty}^{\infty} [\tilde{E}(t') + \tilde{E}(t'-\tau)]^2 e^{-i\gamma_0 \omega t'} dt' \right|^2 . \tag{2.23}$$

A genetic algorithm is used to reconstruct the obtained trace, yielding the spectral amplitude and phase. The obtained spectral phases can be applied via a pulse shaper for full pulse compression.

Active pulse shaping

There is a variety of femtosecond pulse shaping methods [80, 81]. Liquid-crystal displays (LCDs) are widely used but lack the possibility to vary the pulse settings with a kHz repetition rate, which is favorable for rapid data acquisition.

In this thesis, a commercial *acousto-optical programmable dispersive filter* (AOPDF, Dazzler) is employed. The basic principle is that the incoming optical pulse interacts with an acoustical wave in a birefringent TeO_2 crystal via the elasto-optic effect [82]. For the present setup, a detailed description of the working principle is provided by [83].

Briefly, an arbitrary acoustic wave with MHz frequency is generated by a radio-frequency generator and transduced on the crystal along the beam propagation direction. Due to the huge velocity difference between sonic and optical waves, the acoustic wave can be regarded as stationary. In case of phase matching between the optical and the acoustic wave, a part of the respective frequency component is switched from the fast ordinary axis to the slower extraordinary axis. The difference in transmission velocity between the axes enables to generate pulse sequences from a single input pulse that are arbitrary in amplitude and phase. For small radio-frequency intensities, the electric output field is proportional to the electric input field. The extraordinary axis is tilted by an angle of 1° from the optical axis, which may lead to space-time coupling effects for large delays or temporally long pulses [84, 85]. For the given pulse shaper, the acoustic wave takes about 30 µs to propagate through the crystal, which limits the repetition rate to a few kHz. Recently, acousto-optical pulse shapers have been developed that are capable of 100 kHz repetition rates [86].

Rotating frame

The full phase control provided by active pulse shaping enables measuring in a *rotating-frame* environment. The type of frame can be adjusted by γ_0, a frequency scaling factor that has been shown in eqs. (2.9–2.12) and (2.23). In contrast to the *laboratory frame*, where the carrier and the envelope phases of pulses are shifted together in time ($\gamma_0 = 1$), the carrier wave is kept constant when shifting the envelope in the rotating frame ($\gamma_0 = 0$). In the laboratory frame, the system response is convoluted with interference of the excitation pulses, leading to an oscillation of the measured signal in time. In this case, a small step size is required to resolve these oscillations [87, 88].

In order to record only oscillations stemming from the system response [79] and reduce the amount of measurement increments, data acquisition in the rotating frame offers the possibility to significantly reduce the acquisition time.

The signals with a frequency ω then occur at $\omega - \omega_{ref}$. The reference frequency is given by $\omega_{ref} = \omega_0 (1 - \gamma_0)$, where ω_0 is the center frequency of the rotating frame.

For 2D measurements, a value $\gamma_0 = 0$ results in a peak position around the origin. In cases where it is unclear whether a certain nonlinear contribution is unambiguously extracted, one can also apply a partially rotating frame with $0 < \gamma_0 < 1$. The contributions are hereby shifted from the origin to their respective quadrants, enabling distinguishability.

Scan schemes

The usefulness of shot-to-shot sampling for transient absorption spectroscopy has been proven in a direct comparison between various modes of averaging [89]. This demonstrated that measurement times can be reduced dramatically under appropri-

ate conditions, and thus shot-to-shot rapid sampling is also beneficial in 2D spectroscopy.

An insightful analysis of different 2D data-acquisition schemes and the influence on the signal-to-noise ratio and measurement time has been provided by the Zanni group [86]. They found that shot-to-shot data acquisition reduces the measurement time by a factor of 13 for reaching the same signal-to-noise ratio, and attributed this circumstance to the higher correlation between subsequent laser pulses.

3 Experimental implementation

This chapter shall describe the experimental setup and the implementation of existing techniques. The main setup is set out in section 3.1. The implementation and limitations of the used pulse shaper are explained in section 3.2. White-light generation methods via noncollinear optical parametric amplification and filamentation in a hollow-core fiber are compared and qualitatively discussed in section 3.3. In section 3.4, the requirements and possible issues concerning signal detection are considered. Artifacts that can occur due to data analysis, the pulse shaper and the applied photodetector are discussed in section 3.5.

3.1 Experimental setup

The experimental setup is shown in fig. 3.1. Some parts varied for the population-evolution one-quantum experiments (see chapter 4) and the two-quantum experiments (see chapter 5). Nevertheless, the beam path and working principle was the same for all 2D experiments. For clarity, the setup is therefore described in general in this section. When providing values, the respective values for chapter 5 will be given in square brackets.

The laser source was a commercial Ti:Sa amplifier system (Spitfire, Spectra Physics), that generates 120 fs [35 fs] pulses centered at 800 nm with a repetition rate of 1 kHz. 1 mJ [400 µJ] of this beam was used to create white light via noncollinear optical parametrical amplification (TOPAS, Light Conversion), or an argon-filled hollow-core fiber (HCF, UltraFast Innovations), respectively. Optionally, the incoupling of the 800 nm beam could be improved by utilizing an active beam stabilization system (Aligna, TEM Messtechnik GmbH). Active pulse-shaping, including pulse compression and multi-pulse-sequence generation on a 1 kHz shot-to-shot basis was performed with an acousto-optical programmable dispersive filter (AOPDF) (Dazzler, Fastlite). Before entering the Dazzler, the short pulses of variable frequencies had been pre-compressed by a single-prism compressor [1, 79] or a dual grism compressor [2] in order to correct for the positive group-delay dispersion of 20000 fs^2 that is introduced by the Dazzler crystal.

The pulses were characterized and compressed close to the bandwidth limit via pulse-shaper-assisted collinear frequency-resolved optical gating (cFROG) [78]. For the 2D experiments, four-pulse [three-pulse] trains have been generated by the Dazzler and focused into a capillary-type flow cell with square cross section (250 ×

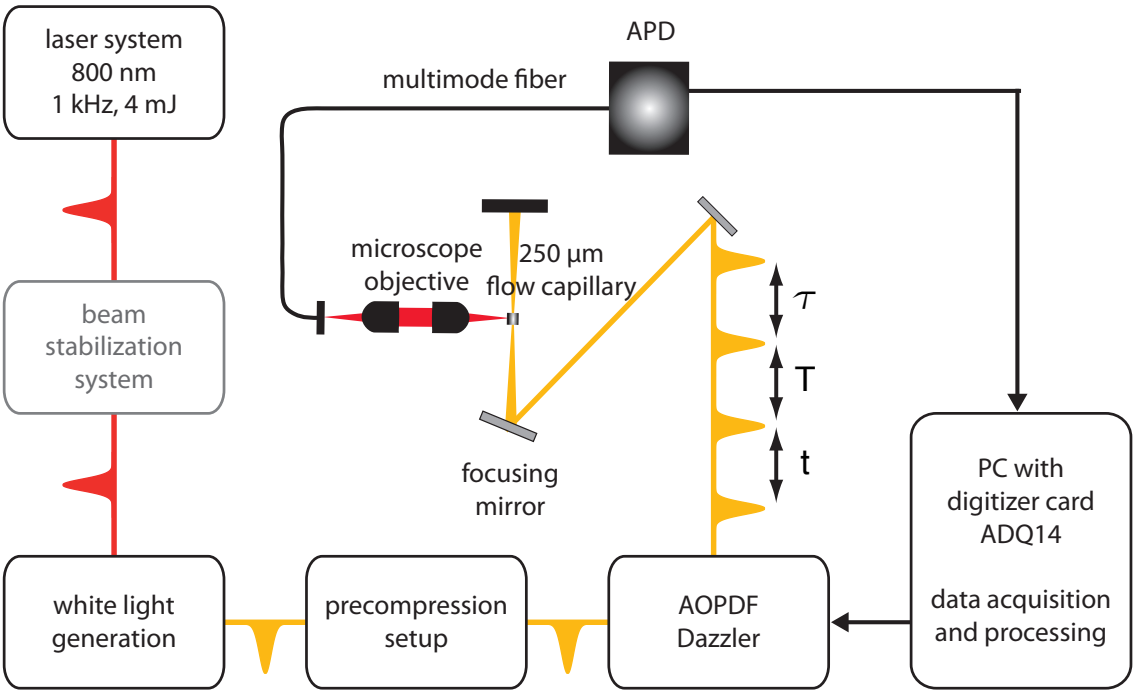

Figure 3.1: General setup. Setup for rapid-scan 2D fluorescence spectroscopy, consisting of a Ti:Sa laser, white light generation via nonlinear optical parametrical amplification (NOPA) or hollow-core fibre (HCf), respectively, a precompression unit (prism or grism compressor), a pulse shaper and an avalanche photodiode (APD). The core item is the pulse shaper based on an acousto-optical programmable dispersive filter (AOPDF), facilitating compression of the incoming pulses as well as the generation of multiple-pulse sequences with arbitrary phases and delays on a shot-to-shot basis. Adapted and modified from [1].

250 µm^2, 131.310-QS, Hellma) and four polished sides, with a focus diameter of 60 µm. The focus diameter has been determined using a web cam. In order to provide fresh sample molecules for each shot, the sample was pumped through the capillary using a micro annular gear pump (mzr-2942-cy, HNP Mikrosysteme GmbH). The actual measurement signal was fluorescence, which has been collected with a combination of two 0.25 NA microscope objectives (04OAS010, CVI Melles Griot) and imaged on a 0.22 NA multimode glass fiber with a core diameter of 400 µm (QP400-2-SR, Ocean Optics). The signal has been measured in a 90° angle with respect to the excitation beam. Since the excitation polarization was set in the direction of the

fluorescence detection, this geometry enabled scattering prevention.

The glass fiber can be used to lead the fluorescence signal to a freely selectable detection device. We used a spectrometer (HR 4000, Ocean Optics) to confirm that only fluorescence signal is detected without scattering contributions from the excitation light. For the 2D measurements, a sensitive avalanche photodiode (APD) (A-Cube S500-3, Laser Components) [APD410A2, Thorlabs] was used while attenuating the signal to a level which was still in the linear detection regime with absorptive neutral density filters (FS-3R, Newport). The signals were digitized with a data acquisition unit (ADQ14, Signal Processing Devices Sweden AB) and processed on a personal computer. The data-analysis process is described in detail in chapter 4.

The setup is fully collinear with no movable parts like, e. g., translation stages, offering an inherent phase stability and an easy alignment.

3.2 Pulse shaper implementation

Pulse shaping plays a pivotal role for this work, since all inter-pulse phases and delays are generated with an AOPDF. The principles of pulse shaping have been described in the previous chapter in section 2.3.2, including active (via the AOPDF) and passive (via prism and grism compression) approaches. In the following, we provide a short software and experimental implementation overview in order to provide the user basis for the 2D experiments in the following chapters 4 and 5.

Shaping window

The maximum delay is limited by the Dazzler crystal size to 8000 fs. This limit can be reached in case of perfectly pre-compressed pulses by prism or grism compression (see section 2.3.2). In this case, however, the peak intensities become very high at a certain position in the Dazzler crystal, decreasing the overall shaping efficiency dramatically. Furthermore, artifacts in the 2D spectrum can occur, deriving from shaper nonlinearities at these peak intensities. These artifacts will be discussed in section 3.5.2. Coherence times in liquid-phase 2D experiments usually decay within few hundreds of femtoseconds or less [6]. Thus, it is not necessary to use the full shaping window of 8000 fs. The optimum solution rather includes a balance between shaping window and shaping efficiency in order to provide both a sufficient delay range and pulse energy. If one wants to investigate longer population times, one could combine two AOPDFs and sample the population time via a mechanical delay stage [90, 91]. That approach offers the possibility of additional polarization pulse shaping at the cost of giving up the single-beam-path geometry and inherent phase stability between all four pulses. Phase drifts could still be compensated automatically in such an arrangement using the pulse shapers [92].

Calibration procedure

The intensity of the acoustical wave at each crystal position has to be calibrated in order to ensure a constant output intensity over the shaping window. The calibration is very sensitive to changes in the beam incoupling and thus the beam path through the crystal. The procedure is described in detail in [83].

Briefly, a second-order phase of -100 fs^2 was applied while all other phase terms were set to zero, and the acoustical wave was moved incrementally through the crystal, corresponding to a movement of the optical output pulse in time. The small phase term grants a high spatial resolution, since the acoustical wave then covers only a small part of the crystal. The output spectra were recorded with a spectrometer, ensuring that the spectral shape was constant and enabling to integrate the spectra for further data processing. The integrated spectra were fitted polynomially, yielding a correction factor for each crystal position. The correction factors were applied via the commercial Dazzler software.

Software implementation

The commercial Dazzler software allows the generation of completely customized and arbitrary wave forms with full amplitude and phase control. It is possible to either apply a constant wave form or to vary the wave forms with a 1 kHz shot-to-shot rate in the advanced sequence mode.

The desired pulses or pulse sequences are defined by the user and transferred to the Dazzler software, where the acoustical waves are calculated that are necessary to realize the desired output. The pulse definition can be carried out numerically or polynomially.

With the numerical working mode, an array with a numerical amplitude and phase for each wavelength is transferred to the Dazzler software. With the polynomial mode, an array with information on the number of pulses, their central wavelength, spectral width, absolute phase and phase coefficients from first to fourth order of the Taylor series in equation (2.22) is transferred to the Dazzler software, out of which the numerical amplitude and phase for each wavelength component are calculated by the Dazzler software. The phase coefficients can be retrieved from a polynomial fit of the experimentally determined phases from cFROG measurements. The precision of the numerical mode is naturally higher, because each wavelength component can be adjusted directly without a polynomial fit as an error source. Nevertheless, it is apparent that significantly less memory is needed for the polynomial transfer, since vastly less values need to be transferred. Given a required wavelength range of > 100 nm with a resolution of 0.2 nm, the numerical approach is quite memory-expensive.

This becomes crucial when not only a specific wave form is supposed to be employed, but sequences of wave forms, as is done in 2D experiments. On a 32 bit

basis we observed that it was possible to stream only < 1000 wave forms with the numerical approach, while with the polynomial approach > 100000 wave forms were feasible. For 2D experiments with phase cycling, a large amount of wave forms have to be streamed continuously. Accordingly, the polynomial approach has been applied for all experiments. The performance of the setup concerning the amount of streamable wave forms can be improved significantly by employing a 64 bit system in the future.

Trigger scheme

In the advanced sequence mode, an exact synchronization is essential for a correct data acquisition. The previously calculated waveforms for a measurement are streamed in a sequence consisting of cycles. The Dazzler sends a trigger every ms, and a gate signal when streaming a sequence, or a cycle, respectively. A logical gate box combines gate and Dazzler trigger, forwarding only the trigger signals when a sequence is streamed. The digitizer card has been programmed such that it records exactly the amount of previously defined waveforms when receiving trigger signals.

3.3 Comparison of white-light generation methods

A tunable pulse source is important for applicability to a broad range of molecules with different absorption frequencies. Which pulse-generation technique is most suitable depends on various parameters which will be discussed in this section.

If one wants to excite multiple electronic transitions at once, a broadband spectrum is indispensable. Increasing the spectral bandwidth additionally offers a higher time resolution.

The spectral shape of the linear excitation spectrum has an influence on the measured 2D spectra. A smooth Gaussian spectral shape facilitates data analysis while it can be difficult to differentiate between peaks deriving from molecular response and those deriving from a modulated excitation spectrum.

The TOPAS offers smooth Gaussian spectral shapes with the drawback of limited broadness due to a naturally limited spatio-temporal overlap in the nonlinear crystal. The HCF offers very broad spectra with non-Gaussian spectral shapes. A possibility of disentangling the influences of molecular response and spectral shape on the 2D spectrum is given by the use of simulations which we present in chapter 5.

Long-term stability is important for data acquisition that requires a high amount of averaging, i. e., for weak signal intensities. This can be ensured by active beam stabilization which we used for the experiments in chapter 5.

We could achieve maximum pulse energies at the sample position of ~ 100 nJ when using the TOPAS, and ~ 60 nJ with the HCF. However, third- (or higher) order nonlinear contributions require a high energy density at the transition fre-

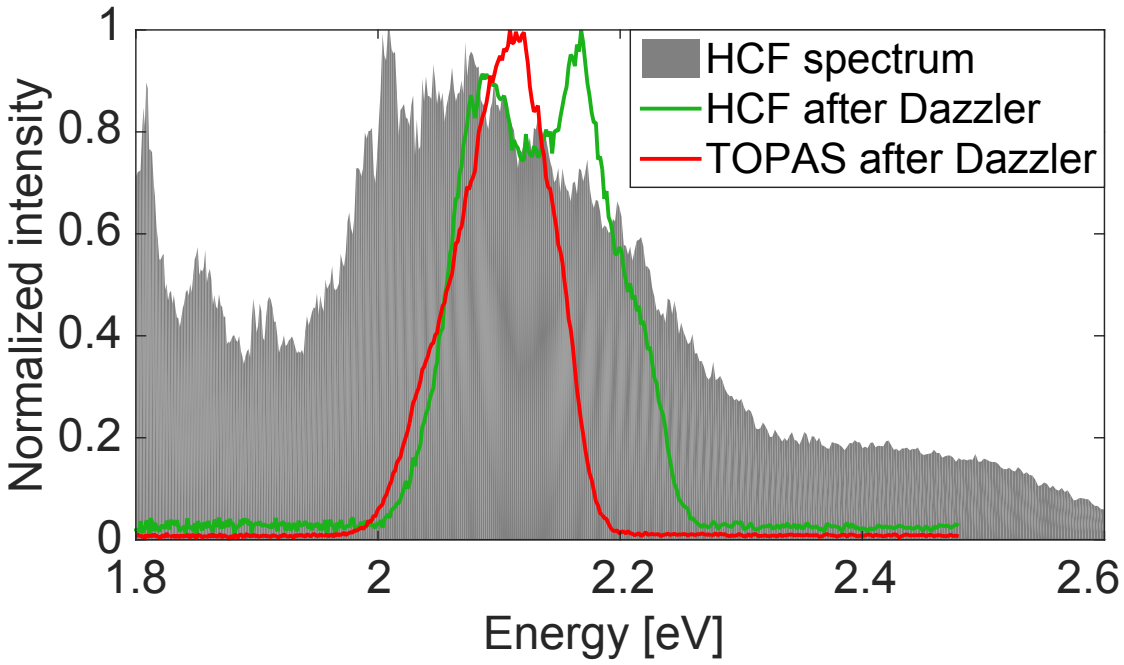

Figure 3.2: Laser spectra. The grey area depicts the HCF spectrum in the visible regime, corresponding to $477 - 689$ nm. The red (green) curve shows the chosen TOPAS (HCF) spectrum after the pulse shaper.

quency. Measuring the pulse energy for a whole spectrum therefore has only limited meaningfulness to determine if the excitation energy is sufficient at the transition frequency.

Figure 3.2 depicts the linear spectra that were generated via TOPAS (red) and HCF (green) after passing the pulse shaper. The total spectral range of the HCF is broader [74], but could not be used completely due to the limited pulse-shaping window of the Dazzler.

Summarizing, the HCF is more suited for experiments where coupling between electronic states is to be observed, as well as for experiments that require a high time resolution, while using the the TOPAS is more appropriate when pulse energies at specific frequencies are needed. In perspective, the HCF will be suitable for multi-color spectroscopy, where a pulse sequence consists of pulses with varying center frequency [93]. Considering two-environment experiments that apply the same pulse sequence to liquid and gas-phase samples simultaneously, pulse generation via TOPAS seems to be the method of choice due to the higher achievable pulse energies.

As mentioned before, the pulse characterization and compression to near-bandwidth limit has been performed via cFROG. Using the Dazzler, a double pulse was created and the delay between the pulses was incremented in 1 fs steps from -300 fs to 300 fs in a partly rotating frame with $\gamma_0 = 0.3$.

3.4 Signal Detection

This section will provide information about the requirements of the detection unit. Furthermore, ensuring detector linearity is described and supported with corresponding measurements that have to be carried out before the 2D experiments.

Detector requirements

The measured incoherent fluorescence signal includes a broad range of signal contributions stemming from the observed molecular ensemble. The desired third-order signal is small compared to the static first-order contribution to the total fluorescence signal. Hence, the dynamic detector range should be as large as possible.

Since the possibility of acquiring all information without averaging in the 2D experiments is desirable, the detector must not be a photon-counting device, but rather detect many photons at once and enable a quantification via signal integration. By integrating over many photons, all of the ensemble responses can be obtained after one shot of each wave form.

The small probe volume of $60 \times 60 \times 250$ μm^3 necessitates a high sensitivity, both absolute and frequency-dependent. This becomes especially important in perspective, when molecules with a low quantum quantum yield or low concentrations are to be investigated. Additionally, a large part of the induced fluorescence signal is lost because one can only collect it from one direction.

We utilized APDs that fulfill the listed requirements; for the experiments presented in chapter 4 we used the A-Cube S500-3 by Laser Components, and for those in chapter 5 the APD410A2 by Thorlabs. We switched to the APD410A2 because it reveals sensitivity also in the UV, which enhances the possible observation spectrum. Additionally it offers a higher dynamic range as will be shown in the following section.

Linearity check

The most precise way to check for detector linearity is to increment the attenuation via a fixed polarizer and a $\lambda/2$-plate which is rotated by an automatized rotation mount and fit the resulting sine curve. The condition for that approach is a polarized light source. Additionally, since every detector has a frequency-dependent sensitivity, the linearity has to be checked in the frequency regime of the fluorescence signal. In order to check for the (non-)linearity in the specific frequency regime of the fluorescence signal, the method is unsuitable due to the isotropic nature of fluorescence. In the optimized fluorescence-collection setup there is no space for two polarizers and a $\lambda/2$-plate, which could circumvent the isotropic issue.

Since for the linearity measurement and the 2D experiment the same geometrical properties are desirable, we chose a different solution, which is not as precise as the automatized approach with respect to the intensity resolution. However, the chosen

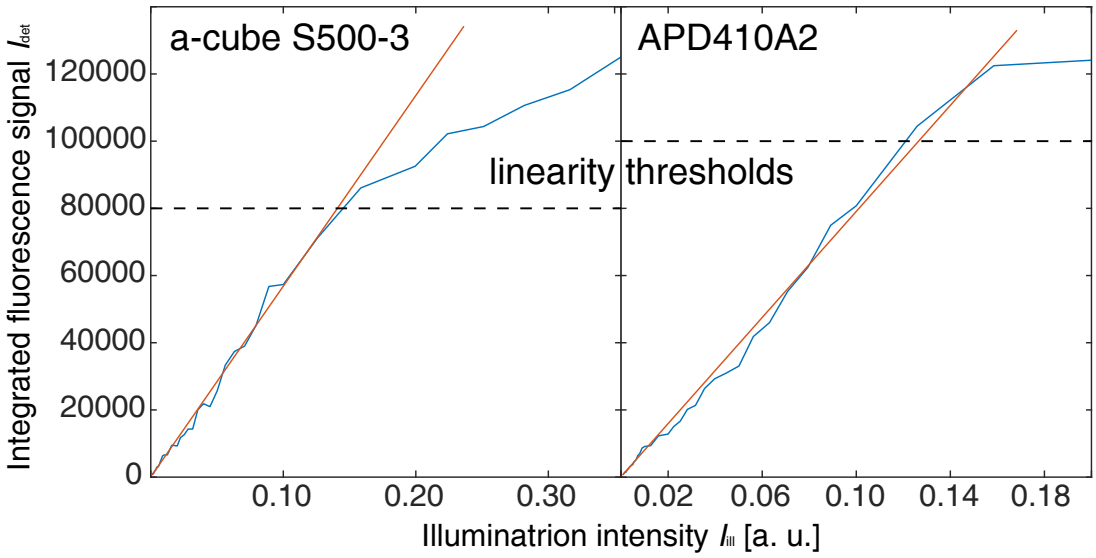

Figure 3.3: APD linearity measurement with fluorescence signal of cresyl violet: Integrated measured signal over calculated relative signal intensity (blue curve) with A-Cube S500-3 (left) and APD410A2 (right). The red lines represent linear fits of the respective linear regimes and the dashed lines indicate the thresholds that mark the border between linear and nonlinear regime.

method probes the linearity for the exact frequency that later is detected in the actual experiment.

For that purpose, the setup was used as described in section 3.1, with the pulse shaper set to a constant radio-frequency (RF) intensity to generate a constant fluorescence intensity of the molecules of interest. The pulse shaper's RF intensity and by that the induced fluorescence intensity was set such that the APD is in the saturation regime, with the digitizer parameters being set to the same values as in the 2D experiments (compare 4.1.2). The linearity measurements were carried out by placing different combinations of absorptive neutral density filters (FS-3R, Newport) between the two microscope objectives for incremental attenuation of the collected fluorescence. For each attenuation increment the intensity at the detector was measured and averaged for 10 s. The resulting linearity curves for the two utilized APDs (A-Cube S500-3, Laser Components and APD410A2, Thorlabs) are provided in fig. 3.3. The x-axis values are calculated relative intensities with 1 for no attenuation with a highly saturated detector. It is apparent that the upper threshold of the linear regime is limited to a value of ~ 80000 and ~ 100000, respectively. A discussion of nonlinear detector effects is provided in section 3.5.3, as well as a suggestion for data correction when measuring beyond the linear regime.

3.5 Artifact sources and correction

There are several artifact sources to consider for fluorescence-detected 2D spectroscopy. This section will list the observed artifacts, explain their origin, and show how to either avoid or correct them.

3.5.1 Fourier-transformation artifact

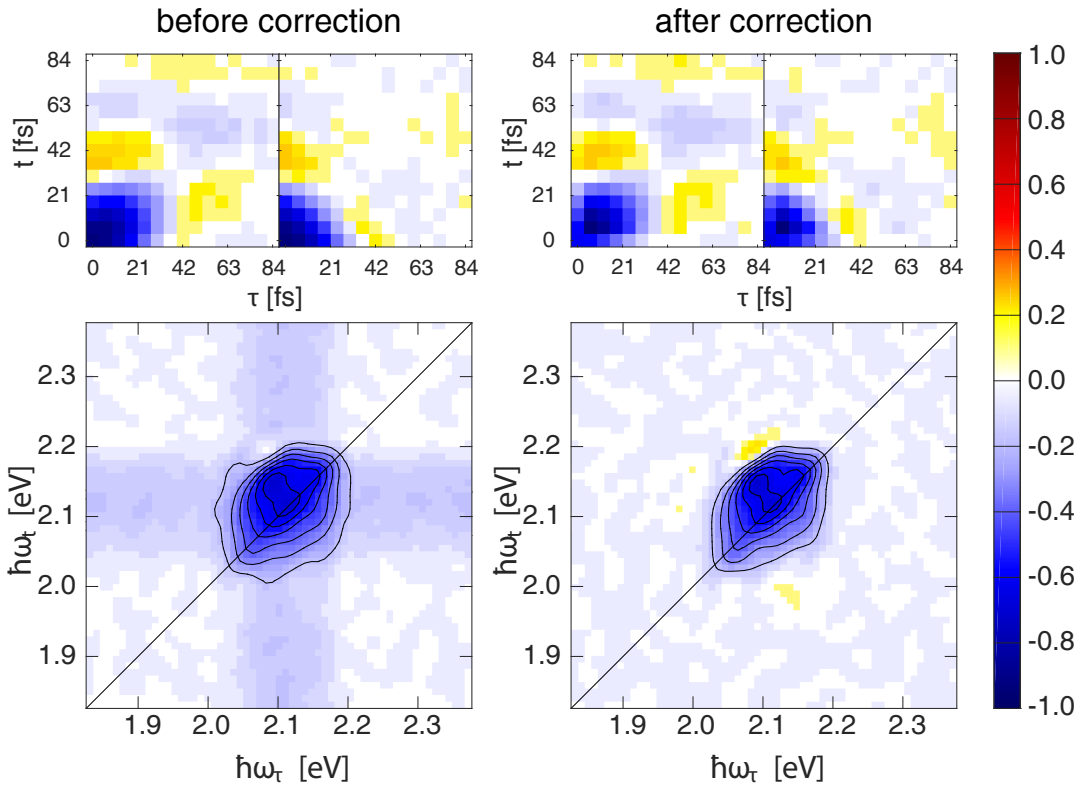

Figure 3.4: Time-domain data correction according to trapezoidal rule [53]. Time domain data of rephasing and nonrephasing 1Q contribution (top) and resulting absorptive 2D spectra (bottom) before (left) and after correction (right). The cross artifact in the absorptive 2D spectrum disappears after data correction, leaving only the features that stem from molecular response. The data is adopted from the experiment in chapter 4.

The following artifact discussion is adapted from a textbook by Hamm [53]. Obtaining 2D frequency spectra from time-domain data requires a subsequent Fourier transformation. Given the finite amount of sampling points N along both coherence time axes τ and t, the Fourier transform is discrete. The measured signals are single-sided response functions which have large values for $\tau = 0$ and $t = 0$ but a value of

zero for $\tau, t < 0$, leading to a strong discontinuity. The effect of this discontinuity is illustrated by the cross artifact in the 2D absorption spectrum on the left side of fig. 3.4. The data is taken from the data set that will be presented and discussed in chapter 4.

Small sampling sizes lead to large artifacts, which is the case for the given sampling size of $N_\tau = N_t = 15$. The resulting cross artifact along both axes is clearly visible and can be attributed to the error of the discrete Fourier transformation as discussed above. It is obvious that there should be no signal along the axes, because there is neither molecular absorption nor laser spectrum at these energies (see fig. 3.2).

In order to account for this effect, we used the trapezoidal rule [94], according to which the first and last summands of the discrete Fourier transform have to be multiplied by 1/2. For the given case, this means applying the correction factor of 1/2 on the time-domain data for all points with $\tau = 0$ and $t = 0$ (i. e. 1/4 for $\tau = t = 0$), visible in the time domain data on the top right of fig. 3.4. The bottom right side of fig. 3.4 illustrates how the cross artifact in the 2D absorptive spectrum disappeared, leaving only the actual signal amplitude $\neq 0$. This correction scheme has been applied for all data analyses in chapters 4 and 5.

3.5.2 Pulse-shaper artifact

Depending on the specific wave-form parameters (i. e. RF intensity and phase coefficients), a characteristic artifact pattern can occur in the obtained 2D spectra.

For illustration, fig. 3.5 a) shows the time (top) and frequency (bottom) domain data of the rephasing contribution for increasing RF intensities from RF= 0.02 to RF=0.10 with a specific wave-form-parameter set. The measurement was carried out on cresyl violet following the procedure described later in chapter 4. When inspecting the time domain data, it is clearly visible that the amplitude in the region for which the nonlinear signal should have decayed cannot be attributed to molecular response, and that this artifact is increasing with increasing RF intensity. The impact on the frequency maps is a narrowing of the signal peak and an introduction of wiggles.

The artifact originates from pulse-shaper nonlinearities as can be shown by simulations of a photodiode response. For that purpose, the spectral interference $E(j, n, m)$ of three pulses in a three-pulse sequence was simulated via

$$E(j,n,m) = \left(E(\omega)e^{-i\phi_{1,j}+\omega} + E(\omega)e^{-i\phi_{2,j}+\omega\tau_n} + E(\omega)e^{-i\phi_{3,j}+\omega(\tau_n+t_m)}\right)^{1.1}, \qquad (3.1)$$

with an identical central frequency ω, their respective phases ϕ_i and coherence times τ and t. Index j describes the phase-cycling increment and indices n and m describe the respective coherence time increments of τ and t. For the 2D map, the spectral interferences were calculated according to the experimental phase-cycling scheme and

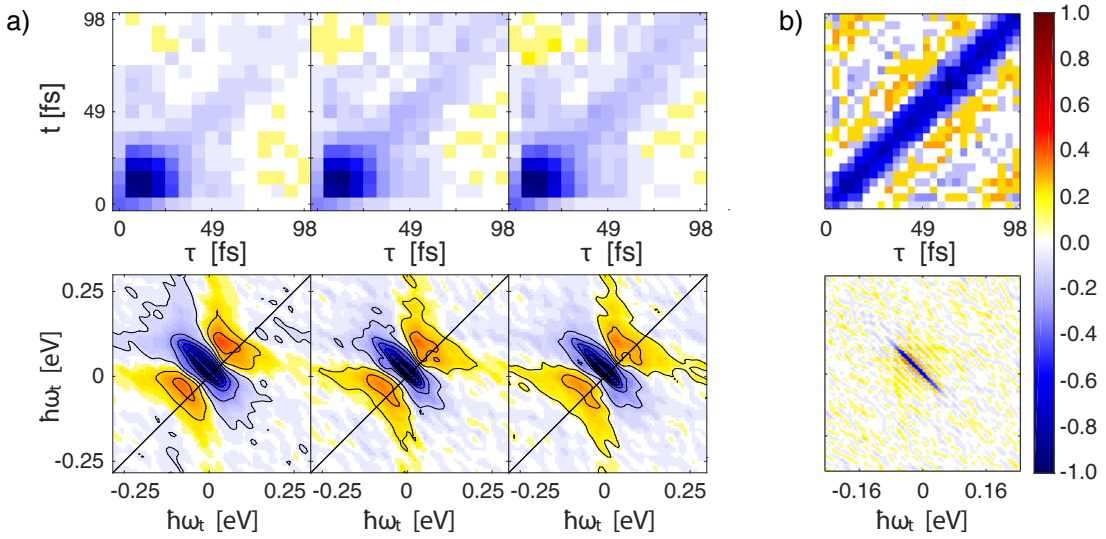

Figure 3.5: a) Pulse-shaper artifact with increasing RF intensity from RF= 0.02 (left) to RF= 0.10 (right). The diagonal artifact in the time-domain maps increases (top), causing a spectral narrowing and the introduction of wiggles in the frequency-domain maps (bottom). The spectra are individually normalized to their maximum absolute value. b) Simulation of a photodiode response to the respective pulse sequence including pulse-shaper nonlinearity.

coherence-time incrementation. The intensity I_{det} at the detector was modeled via

$$I_{det}(j,n,m) = \sum_{j,n,m} E(j,n,m) \cdot E(j,n,m)^*. \tag{3.2}$$

The red-marked exponent in eq. (3.1) is responsible for the artifact in the simulated 2D maps that are shown in fig. 3.5 b). Without that exponent, one would expect perfect cancellation of the photodiode responses after weighting.

The RF dependency suggests that it is desirable to keep the RF intensity to a minimum. There are two issues with that argumentation, though. First, even with very low RF intensities there can be a dominant artifact, depending on the other parameters. This especially holds for the case of high peak intensities in the Dazzler crystal, i. e., when the phase coefficients have low values. However, low phase coefficients are desirable in order to obtain a maximum delay-shaping window. Second, one often needs a high excitation energy and thus a high shaping efficiency in order to observe a nonlinear molecular response in population-based 2D spectroscopy.

In cases where it is not possible to keep the RF intensity low enough to avoid the pulse-shaper nonlinearities while still being able to obtain the desired nonlinear signal, it is necessary to correct the artifact. Our observations show that this especially

applies when using the HCF due to the lower pulse energy at specific frequencies when compared to the TOPAS.

One possibility for artifact correction is an amplitude correction for each pulse combination in a 2D pulse sequence [83]. However, this method is very time-consuming in the common case where there are several thousand different wave forms that have to be corrected.

Another possibility is the acquisition of an additional 2D data set where the excitation pulses are attenuated by a high factor of, e. g., 1000 before the sample, but after the pulse shaper [95]. This low-power measurement can then be taken as a reference to subtract the artifact from the high-power measurement. The idea is that the pulse-shaper nonlinearities are the same in both measurements while the nonlinear molecular response can only be obtained by the high-power measurement. The intensity at the detector has to be the same in order to exclude additional detector-related artifacts (see next section). This circumstance requires a highly sensitive detector, because it diminishes the effective sensitivity for the complete measurement including the correction by the attenuation factor above.

For the results that are presented in this work, none of the two correction schemes have been applied. In the 1Q experiments in chapter 4 the artifact was negligibly small thanks to a high pulse energy from the TOPAS and consequently low necessary RF intensities. The artifact could also be neglected for 2Q spectroscopy in chapter 5 because experimentally it is only visible in the rephasing 1Q contribution. Nevertheless, the correction schemes might be useful for future experiments and therefore are pointed out for the sake of completeness.

3.5.3 Detector artifact

Especially for weak nonlinear signals like the 2Q contribution it is important to ensure that the acquired signals originate from the molecular response. It can be shown that detector artifacts can occur that resemble the desired molecular response.

The origin of this effect can be simulated by calculating all spectral interferences for a pulse sequence analogously to eq. (3.1) without an exponent as follows:

$$E(j,n,m) = \left(E(\omega)e^{-i\phi_{1,j}+\omega} + E(\omega)e^{-i\phi_{2,j}+\omega\tau_n} + E(\omega)e^{-i\phi_{3,j}+\omega(\tau_n+t_m)}\right), \tag{3.3}$$

The nonlinearity of the detector intensity I_{det} is then introduced by the exponent marked in red via

$$I_{det}(j,n,m) = \left(\sum_{j,n,m} E(j,n,m)\cdot E(j,n,m)^*\right)^{0.9}. \tag{3.4}$$

It is therefore of immense importance to stay in the linear detector range. As an additional test if the signal in measured 2D spectra originates from the mea-

sured molecules, one can perform high- and low power measurements as described in the precedent section 3.5.2. A comparison of the non-normalized weighted 2D signals should reveal that the high-power measurement exhibits higher absolute signal amplitude, with the optimum case that there is only noise in the low-power measurement. Following this procedure, we validated that the data in chapter 5 originated from the molecules and supported this conclusion with simulations. For the data presented in chapter 4, we took the reproduction of a reported quantum beating frequency as proof that the signals indeed stemmed from molecular response and not a saturated detector.

However, for very weak signal contributions or for molecules, where multiple averaging is not possible due to a high degradation rate, obtaining these contributions while staying in the linear detector regime may not always be possible. As will be shown in the following chapter, most of the signals in a 2D measurement are far away from the nonlinearity threshold, if the maximum signal of a measurement is adjusted such that it is close to this threshold. Enhancing the intensity of the major part of signals closer to the threshold potentially increases the signal-to-noise ratio with the drawback of partial nonlinear detector effects.

We therefore suggest a correction scheme for the raw data. During a 2D measurement a signal $p(\tau, T, t, \beta, \gamma, \delta)$ is acquired with a specific intensity at the detector $I_{det}(p)$ for each pulse combination.

As shown in fig. 3.3, the integrated fluorescence signal at the detector I_{det} can be plotted against the illumination intensity I_{ill}, which corresponds to the actual intensity at the detector with arbitrary unit. The first step of the correction procedure is to apply a linear regression to the linear regime of the linearity curve I_{det}, yielding the equation for the optimum intensity $I_{lin}(I_{ill})$ at the detector in the linear case. Additionally an appropriate fit (e. g. polynomial) is applied to the nonlinear regime of the linearity curve, yielding $I_{det}(I_{ill})$.

The dependency can be inverted to $I_{ill}(I_{det})$ by swapping the axes and again fitting the resulting curve with an appropriate fit function. For every measured signal $I_{det}(p)$ in a 2D experiment it is then possible to determine the expected illumination intensity I_{ill}, with which the corrected signal value can be obtained by inserting into the linear fit equation $I_{lin}(I_{ill})$.

3.6 Summary

We presented a setup for single-beam fluorescence-detected 2D spectroscopy with no movable parts like, e. g., mechanical delay stages. The single-beam geometry offers the advantage of compactness, inherent phase stability and ease of alignment. The collinear excitation-pulse sequences can be arbitrarily generated with a commercial AOPDF on a 1 kHz shot-to-shot basis. We discussed the implementation of the pulse shaper, and concluded that a polynomial phase adjustment is beneficial in the current

setup configuration for shot-to-shot pulse-sequence variation. White-light generation via NOPA and HCF has been compared and their respective advantages concerning spectral broadness and pulse energies have been evaluated. For fluorescence detection, we determined the dynamic detector range. Finally, artifact sources have been identified that may arise from different sources, including data processing, the pulse shaper and the detector, and correction procedures for all artifact types have been provided.

4 One-Quantum Two-Dimensional Spectroscopy

As a proof-of-principle experiment, a 2D measurement series was conducted using commercially available cresyl violet (Radiant Dyes GmbH) in ethanol with a concentration of 0.1 mM at ambient conditions. Cresyl violet is a well-characterized laser dye that exhibits an oscillatory behavior during the population time. Ultrashort pulses were generated by the TOPAS and shaped to pulse sequences via the Dazzler. As discussed in section 3.3, the TOPAS offers a stable and intense white-light generation with the drawback of a limited bandwidth compared to a HCF. The TOPAS bandwidth is not sufficiently broad to access different electronic states, but enough to access the vibrational sublevels that are responsible for the oscillatory behavior of cresyl violet. Consequently, a four-pulse sequence is well suited in order to validate the technique. For clarity, the whole data acquisition and analysis process is described in section 4.1. A major advantage of the presented setup is the rapid data acquisition granted by 1 kHz shot-to-shot pulse incrementation via the Dazzler and signal detection via an APD. The opportunity of acquisition-time reduction is discussed quantitatively in section 4.2, followed by a summary of the findings in section 4.3. The results of this experiment have been published in Optics Express [1].

4.1 Data acquisition and analysis

Since there are several steps between data acquisition and final analysis, it seems vital to list every step in order to identify possible error sources as well as to ensure reliable and reproducible results. Possible error sources are of interest for the identification and correction of artifacts, which have been discussed in section 3.5.

4.1.1 Experimental parameter settings

As set out in section 2.2.2, a $1 \times 3 \times 3 \times 3 = 27$-fold phase-cycling scheme is needed in order to obtain the rephasing and nonrephasing 1Q nonlinear contributions in a four-pulse 2D experiment. The phase differences $\Delta\phi_{i1}$ between pulse i and pulse 1 were cycled through 0, $2/3\pi$ and $4/3\pi$. The number of sampling points along the coherence time axes τ and t could be significantly reduced by employment of a rotating-frame environment while still fulfilling the Shannon-Nyquist limit (see

section 2.3.2). The data acquisition in a completely rotating frame with $\gamma_0 = 0$, centered at the excitation spectrum maximum at 2.10 eV, enabled us to sample the coherence times in 15 steps of 6 fs from 0 to 84 fs, yielding a total of 225 wave forms for coherence-time scanning. Combined with the 27 phase-cycling steps this resulted in 6075 different wave forms for a complete 2D spectrum. Additionally, the time evolution during population time T was measured in 31 steps of 10 fs from 0 to 300 fs. Consequently, the entire 2D data set was covered by a total of 188325 different pulse combinations. For improvement of signal-to-noise, the measurement has been repeated 400 times for averaging. Shot-to-shot temporal pulse shifting and phase cycling was performed by the Dazzler with a 1 kHz repetition rate. The acquisition time for a 2D spectrum including all nonlinear contributions at one population time thus took 6 s and 3 min for all 31 population-time increments.

4.1.2 Fluorescence signal

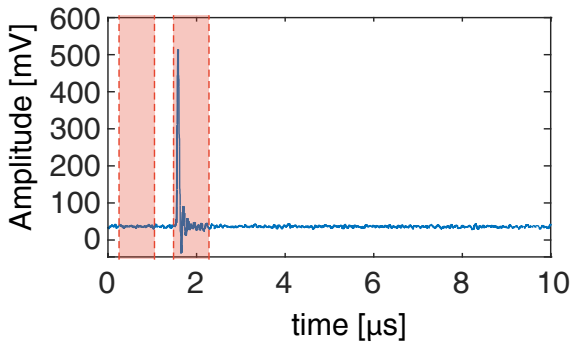

Figure 4.1: Fluorescence signal decay in time after molecule interaction with an exemplary single pulse sequence. The red highlighted areas correspond to the ROIs with a size of 8 µs for noise background (left) and fluorescence signal (right).

The fluorescence intensity of the investigated molecules after interacting with a multi-pulse sequence is depending on the phase relations of and time delays between the pulses of this multi-pulse sequence. The fluorescence signal has a certain lifetime and since fluorescence-signal integration rather than photon counting has been applied in this work, it is worth to take a look at the fluorescence decay in time. Figure 4.1 shows an exemplary APD (A-Cube S500-3, Laser Components) signal of fluorescence decay in time after the ensemble interaction with an exemplary pulse sequence.

In order to determine the fluorescence intensity, two regions of interest (ROIs) were selected, with the background ROI (left) being subtracted from the peak ROI

(right). The ROIs had the same size of 0.8µs, ensuring that the whole signal was included. The background-free fluorescence signal was integrated and used for further processing.

It is vital that the integrated signal lies below the nonlinearity threshold of the detector which has been obtained as described in section 3.4. For intensity adjustment at the APD, a pulse sequence with maximum pulse overlap has been applied to the molecular sample, corresponding to the maximum pulse intensity during the 2D experiment. This maximum fluorescence signal intensity was then attenuated with neutral density filters ($OD = 2.6 - 3.0$, depending on the excitation-pulse energy) to below the threshold of 80000. Note that the necessity of attenuating the fluorescence signal of cresyl violet implies the applicability of the setup to fluorophores with a far lower fluorescence quantum yield or with lower concentrations. For a similar concentration and in case of a similar extinction coefficient at the excitation frequency, this means that a fluorescence quantum yield of down to 0.05% would be sufficient to be detected with the present setup, given the cresyl violet fluorescence quantum yield of $\approx 50\%$ [96]. Peak jittering is determined to be not measurable with the time resolution of the digitizer card and thus can be neglected.

4.1.3 Raw time domain data

The time-domain data acquisition is naturally carried out in a one-dimensional fashion, meaning that all different increment steps are acquired in a row. For all 2D experiments in this work, the incrementing is the same: first the phase cycling, second the coherence time scanning, third the population time scanning (only in the current chapter), and finally the repetition of the scheme in order to improve data quality via averaging. As described in section 2.3.2, this scheme ensures the most economic data acquisition.

Since most of the signal is located around the origin of a 2D spectrum, a quadratic instead of a linear coherence-time scanning can further improve the signal-to-noise ratio per measurement and thus reduce the acquisition time. The quadratic scan scheme is illustrated in fig. 4.2, where $i|j$ refers to the delay combination of τ_i and t_j. Every additional increment along both axes improves the spectral resolution. A detailed evaluation of error evolution is carried out in section 4.2.

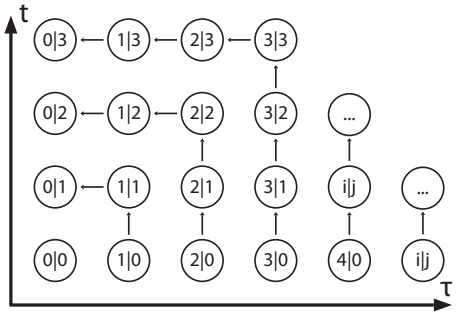

Figure 4.2: Quadratic scan scheme.

Figure 4.3 a) shows the one-dimensional raw data set for all 31 population times. The inspection of this data is important to check whether all values are in the linear regime of the detector (see sections 3.4 and 3.5.3). It is apparent that the data is in the

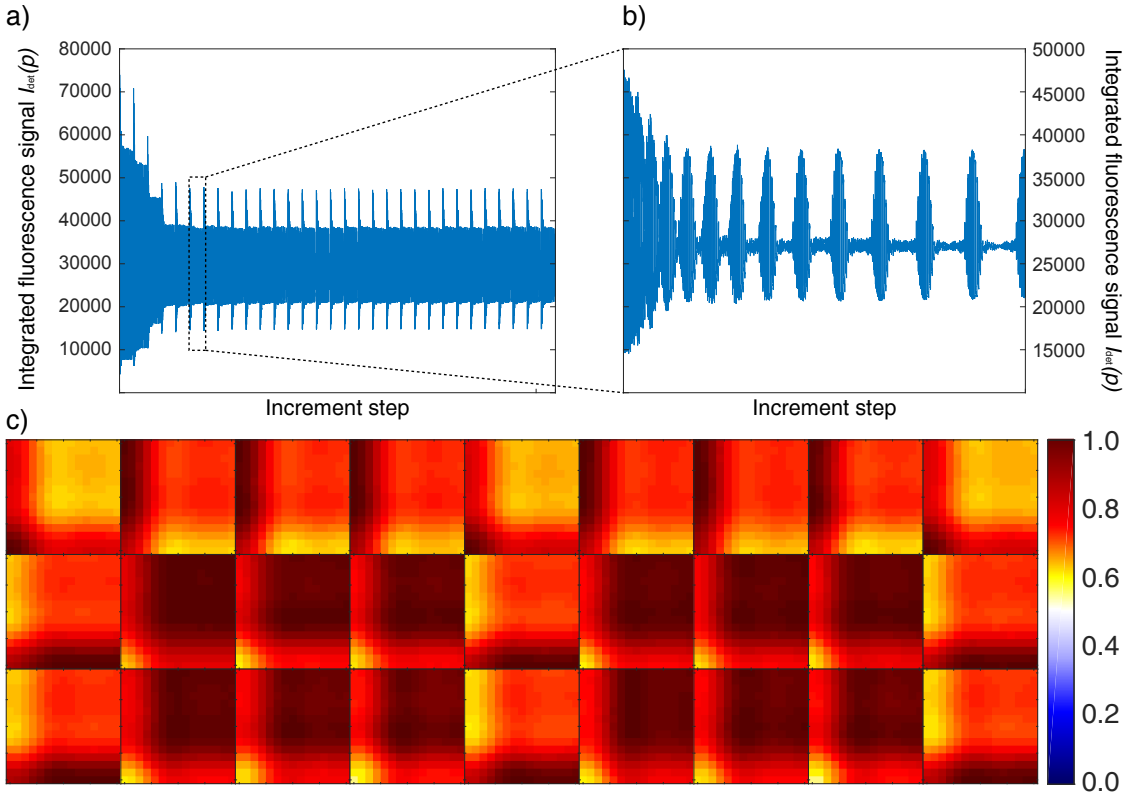

Figure 4.3: Raw data of integrated fluorescence signals. a) 1D raw data of the complete data set using the most economic scan scheme after averaging 400 × before reshaping to 2D spectra. The x-axis corresponds to the increment step, the y-axis corresponds to the respective integrated signal intensity. b) Raw data for an exemplary population time $T = 50$ fs. It is apparent that the integrated signals are well below the nonlinearity threshold. c) 2D raw data for population time $T = 50$ fs. The single maps correspond to the 27 phase-cycling steps with coherence time τ on the x-axis and t on the y-axis. Note that the signal is relatively high for all increments due to the lack of negative interference contributions in fully rotating-frame environment.

linear regime; a large part of the data is even far below the nonlinearity threshold and closer to the noise floor than to the nonlinear regime. It has to be considered that most of the obtained fluorescence signal derives from an interaction of molecules with pulses that are not in the desired time-ordering or with a number of pulses $\neq 4$. The fluorescence signal stemming from the desired fourth-order populations, that are induced by light-matter interaction with the defined pulse sequence in the right time ordering, are significantly less intense and lie on top of this static fluorescence. If the

signals are too close to the noise floor, the desired signal may become negligibly small and hard to extract. For the sake of a beneficial signal-to-noise ratio it is therefore important to make use of the whole linear detector range. This circumstance has to be considered when adjusting the fluorescence attenuation in front of the detector. As apparent from fig. 4.3 a) and b), the linearity range has not completely been exploited for later population times. For weak contributions, one could therefore also go beyond the linear regime for small population times in order to use the full linear detector range for higher population times. The data part that is affected by detector nonlinearity can then either be dismissed or corrected as discussed in section 3.5.3.

Reshaping the one-dimensional data set into $27 \times 31\times$ two-dimensional data sets yields the time-domain data for each phase-cycling and population-time increment. Figure 4.3 c) shows the 27 phase-cycling maps at $T = 50$ fs. The values of the individual pixels are relatively high due to the fully rotating-frame environment. As described in section 2.3.2, a fully rotating frame reduces the oscillating signal decay to a simple signal decay to the static fluorescence baseline.

4.1.4 Phase-cycled 2D maps in time and frequency

Weighting the phase-cycling steps according to eq. (2.17) yields the rephasing ($\beta = -1$, $\gamma = 1$ and $\delta = -1$) and nonrephasing ($\beta = -1$, $\gamma = 1$ and $\delta = -1$) contributions in time domain. Note that the data becomes complex-valued due to the discrete Fourier transformation of the phase-cycling procedure. The respective absolute-valued, real and imaginary parts of these contributions are shown in fig. 4.4 a). A signal concentration at the origin for both the rephasing and nonrephasing contribution is apparent, substantiating the benefit of a quadratic coherence-time scan scheme.

After data correction according to the trapezoidal rule as described in section 3.5.1, the weighted time-domain data is Fourier transformed with five-fold zero padding, yielding the 2D frequency domain spectra shown in fig. 4.4 b). The measurement in the fully rotating frame, centered at 2.10 eV, which corresponds to the maximum of the excitation spectrum, leads to a location of the 2D spectrum around the origin. The peak sign of the real part is negative, resulting from an odd amount of interactions from the right side of the Feynman diagram as discussed in section 2.2.2.

4.1.5 2D absorptive spectra and time evolution

The purely absorptive 2D spectrum for each population time is obtained by summing up the real parts of the rephasing and nonrephasing contribution after an inversion of the $\hbar\omega_\tau$ axis of the rephasing contribution. In order to evaluate physically meaningful peak positions, the spectra have to be shifted by 2.10 eV. This corresponds to the center of the rotating frame and enables a direct comparison with measurements that have been carried out in the laboratory frame. A selection of absorptive 2D spectra

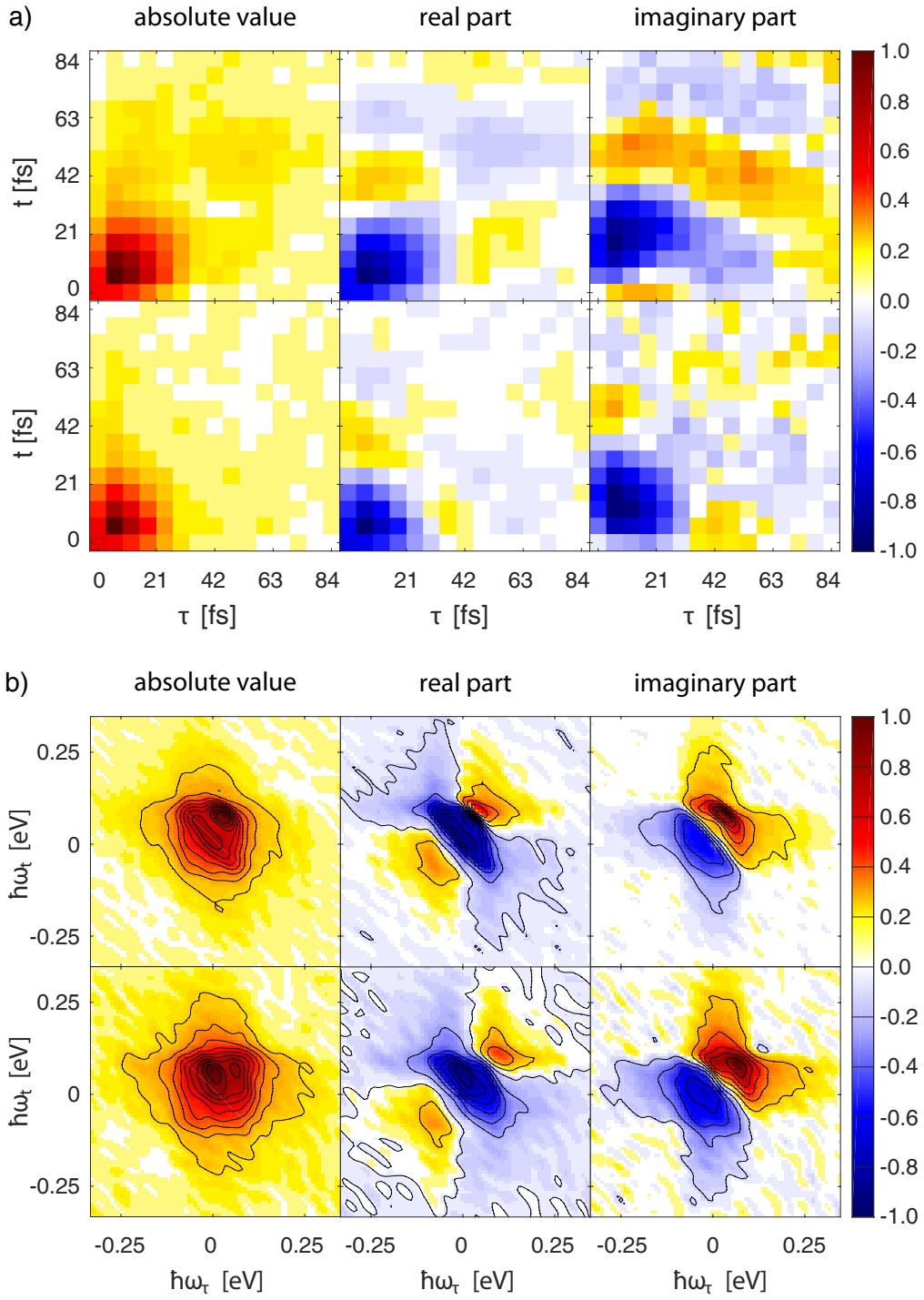

Figure 4.4: Absolute-valued, real-valued and imaginary 2D maps of rephasing (top) and nonrephasing (bottom) 1Q contributions after phase cycling in time (a) and frequency domain (b).

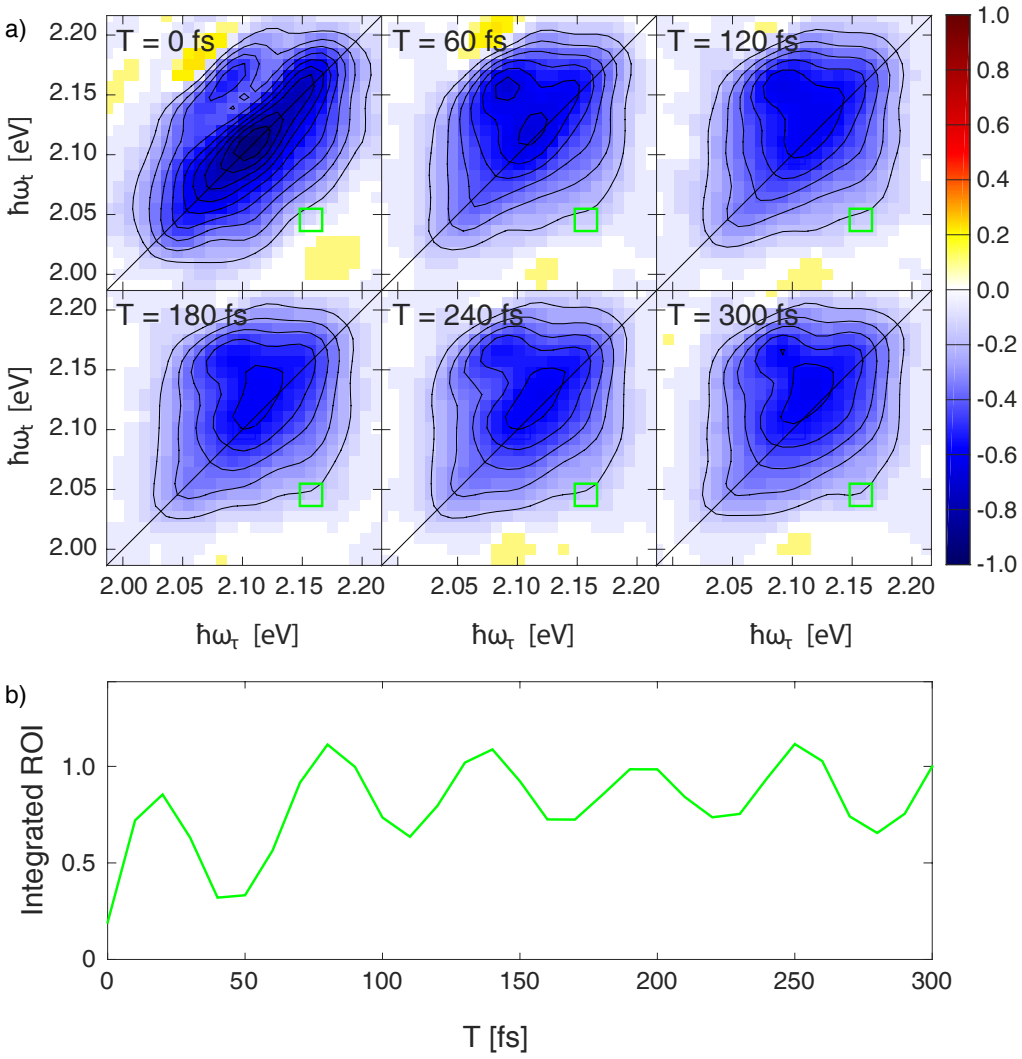

Figure 4.5: a) Purely absorptive 2D spectra at selected population times (0 fs, 60 fs, 120 fs, 180 fs, 240 fs, 300 fs). The spectra are normalized to the maximum absolute value of the absorptive map at $T = 0$ fs. b) Time evolution of the signal integrated over the region of interest marked with a green square in a). Adapted and modified from [1].

for varying population times are shown in fig. 4.5 a). We observe an off-diagonal beating behavior. The oscillations can be analyzed by integrating a region of interest for each population-time step, an example of which is given in fig. 4.5 b). Fourier transform of this oscillation yields a wavenumber of 625 cm^{-1}. Similar frequencies of 585–595 cm^{-1} have been reported in literature [74, 97–100] and can be attributed to a Raman mode of cresyle violet [101].

4.2 Error evolution

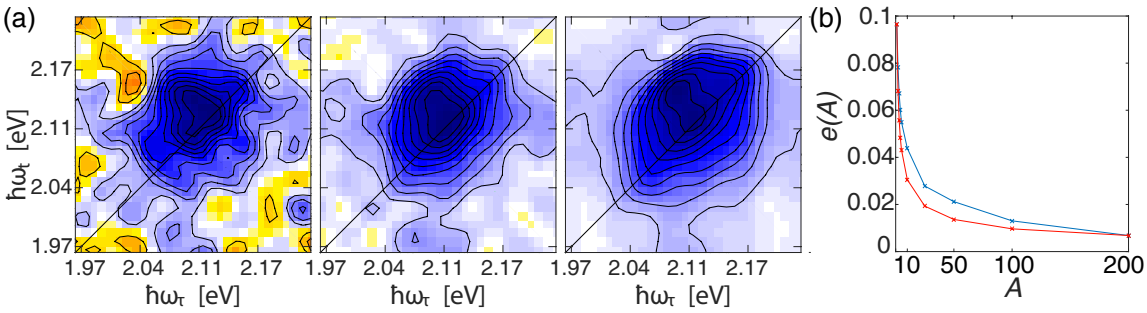

Figure 4.6: a) Absorptive 2D spectra at a population time of $T = 50$ fs for varying amounts of averaging, from left to right: 1×, 10×, 400×, normalized individually for each plot to the maximum value. The normalization factor is further adjusted in the evaluation of the error for each A such that $e(A)$ is minimized. The color code is used analogously to fig. 4.5. b) Error $e(A)$ of the absorptive 2D maps for various amounts of averaging A with respect to the absorptive 2D map using $A = 400$ as a reference (blue) and expected errors for Gaussian statistics with $e(A) = \frac{e(A=1)}{\sqrt{A}}$ (red). Adapted and modified from [1].

The precedent analysis has been conducted with a data set that has been averaged 400 times. Less averaging is also possible, though, and thereby a significant decrease of data-acquisition time. In order to evaluate the signal-to-noise-ratio evolution with increasing averaging steps, we assumed that the data set with 400× averaging has a negligible error, thus constitutes the optimum result and therefore can be taken as a reference for the error evaluation. The quantitative error of a 2D spectrum consisting of $X \times X$ pixels with an amplitude of x_{ij} in column i and row j after A-fold averaging can then be calculated via

$$e(A) = \left[\frac{1}{X^2} \sum_{i,j=1}^{X} |x_{ij}(A) - x_{ij}(A = 400)|^2 \right]^{1/2} . \tag{4.1}$$

Figure 4.6 a) shows 2D spectra at a population time of 50 fs for different amounts of averaging. Even without averaging (left) the relevant features of the 2D spectrum are visible already. Applying eq. (4.1), the error evolution of 2D spectra as a function of averaging steps is depicted as a blue curve in fig. 4.6 b). The red curve represents the expected error evolution for Gaussian statistics. 10-fold averaging is sufficient to obtain an error of < 0.05. Taking into account the acquisition time of 6 s for a single 2D spectrum, this yields a measurement time of 10×6 s $= 1$ min for all

15×15 coherence times and 27 phase-cycling steps. This constitutes an improvement in acquisition time by a factor of 40 compared to an acquisition time of 400×6 s = 40 min, while still obtaining the same information.

4.3 Summary

A detailed description of data acquisition and analysis has been presented for a collinear fluorescence-detected 2D setup. Employing phase cycling enabled us to gather various contributions from one single data set. Literature values of quantum-beating behavior of cresyl violet could be reproduced, yielding a wave number of 625 cm^{-1}. By using the rotating-frame environment and 1 kHz shot-to-shot pulse incrementation, it was possible to obtain a 2D spectrum in 6 s. The error evaluation revealed that 1 min of acquisition time (10× averaging) is sufficient to obtain a root-mean-square error of < 0.05 compared to 400× averaging. The rapid data acquisition makes this method suited for molecules that undergo fast degradation.

5 Two-Quantum Two-Dimensional Spectroscopy

Having proven that the setup is working in chapter 4, we extended it to broadband excitation by utilizing an argon-filled hollow-core fiber for white-light generation. Using a broadband excitation enables to excite more electronic transitions at once and additionally improves the time resolution which is important to resolve fast-oscillating signals like 2Q coherences. A three-pulse sequence with 16-fold phase cycling has been applied on cresyl violet (Radiant Dyes GmbH) in ethanol with a concentration of 0.1 mM at ambient conditions in order to measure 1Q, 2Q and 1Q-2Q coherence contributions at once. The experimental parameters are described in section 5.1. We show and discuss the first fluorescence-detected 2Q experiment and the first experimental data of a 1Q-2Q contribution in section 5.3. The results are validated with simulations in section 5.3, and the effects of the excitation spectrum and relaxation-channel distribution on line shapes and the general interpretation of 2D spectra are discussed in section 5.2. Both 2Q contributions and simulations are used for the determination of the correlation energy Δ. The results and findings have been published in the Journal of Physical Chemistry Letters [2].

5.1 Experimental parameter settings

The general data acquisition and analysis procedure followed the description in chapter 4. Given the application of a three-pulse sequence instead of a four-pulse sequence, we here used a $1 \times 4 \times 4 = 16$-fold phase-cycling scheme in order to obtain the rephasing 1Q, 2Q, and 1Q-2Q contributions simultaneously [62]. The phase differences $\Delta\phi_{i1}$ were cycled through 0, $1/2\pi$, π and $3/2\pi$. 2Q coherences oscillate with double the frequency of 1Q coherences, demanding a higher sampling rate of the coherence times τ and t. We therefore incremented τ and t in 31 3 fs steps from 0 to 90 fs each while measuring in a completely rotating-frame environment. The pulses had a center frequency of 2.10 eV with a duration of 12 fs, determined via cFROG. The excitation spectrum is shown in fig. 5.1 a). A complete data set containing the mentioned nonlinear contributions took 16 s of acquisition time. However, since the 2Q and 1Q-2Q contributions exhibit an overall smaller signal strength than the 1Q contribution and for improvement of data quality, we performed 2000$\times$ averaging.

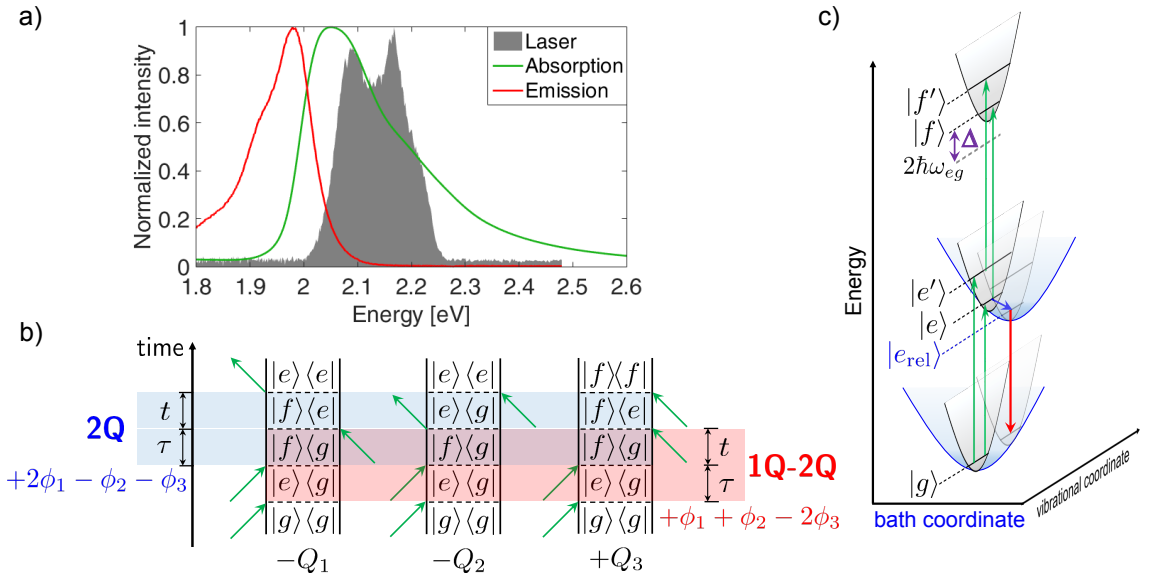

Figure 5.1: a) Linear absorption (green) and fluorescence (red) of cresyl violet perchlorate (0.1 mM) in ethanol (absorption maximum at 2.06 eV, fluorescence maximum at 1.98 eV). The excitation spectrum (grey) was measured behind the AOPDF. b) Energy level scheme of a model system with electronic states $|g\rangle$, $|e\rangle$, $|f\rangle$, vibrational sublevels $|e'\rangle$ and $|f'\rangle$, and $|e_{\mathrm{rel}}\rangle$ corresponding to the relaxed state from which fluorescence (red arrow) occurs after solvent-shell relaxation. Possible excitations are indicated by green arrows. $\Delta = \hbar\omega_{fg} - 2\hbar\omega_{eg}$ is the correlation energy. c) Feynman diagrams for 2Q (blue) and 1Q-2Q (red) Liouville pathways. Adopted and modified from [2].

5.2 Simulations

A drawback of the broadband HCF excitation is the non-Gaussian spectral shape as mentioned in section 3.3. In order to distinguish between molecular features and features deriving from excitation spectrum, simulations can deliver important insights. Furthermore, a quantitative interpretation of experimental findings is enabled.

For theses purposes, we solved for different electronic systems the Lindblad quantum master equation [102], according to eq. (2.4),

$$\frac{\partial}{\partial t}\rho(t') = -\frac{i}{\hbar}\left[H(t'), \rho(t')\right] + \sum_j \frac{1}{T_j}\left(\mathcal{L}_j\rho(t')\mathcal{L}_j^\dagger - \frac{1}{2}\mathcal{L}_j^\dagger\mathcal{L}_j\rho(t') - \frac{1}{2}\rho(t')\mathcal{L}_j^\dagger\mathcal{L}_j\right), \quad (5.1)$$

with the time-dependent density matrix $\rho(t')$, Lindblad operators $\mathcal{L}_j^\dagger$ and $\mathcal{L}_j$, and time constant T_j of a specific dissipation process j. $H(t')$ is expressed as the sum of a time-independent Hamiltonian $H_0 = \hbar\omega_m \sum_m^M |m\rangle\langle m|$ and an interaction Hamiltonian $H_I(t') = \gamma_{ex}E(t)\sum_{m\neq n}\gamma_{mn}\left(|m\rangle\langle n| + |n\rangle\langle m|\right)$, where the overall coupling γ_{ex} of the external field $E(t)$ was set to 0.015. Parameter γ_{mn} describes the transition strength between a pair $|m\rangle$ and $|n\rangle$ and was partly extracted from the linear absorption spectrum and partly used as a parameter to adjust the simulations.The Lindblad operators $\mathcal{L}_j^\dagger$ and $\mathcal{L}_j$ account for environmental effects via dephasing and population relaxation. The simulations have been carried out using a program package in MatLab R2017b that had been programmed by Tristan Kenneweg and modified by Matthias Hensen and Stefan Mueller.

The influence of pathway cancellation on the distinction ability between 2Q and 1Q-2Q spectra is discussed in subsection 5.2.1. Subsection 5.2.2 provides information about simulation parameters and model assumptions for the simulations that are used to interpret the experimental results in section 5.3. In subsection 5.2.3, the influence of the excitation spectrum on simulation results is examined and compared with experimental results in order to further optimize the simulation method to fit the experimental data.

5.2.1 Influence of fluorescence quantum yield

Figure 5.1 b) illustrates Feynman diagrams of possible 2Q and 1Q-2Q Liouville pathways in an electronic three-level system with a ground state $|g\rangle$, an excited state $|e\rangle$ and a two-quantum state $|f\rangle$. Inspection of the pathways Q_1, Q_2 and Q_3 leads to several conclusions:

First, pathways Q_1 and Q_2 end up in a population of $|e\rangle$, while pathway Q_3 has a final population of $|f\rangle$. Considering Kasha's rule, the fluorescence should only occur from $|e\rangle$ for most molecules [66]. Thus, the final population of Q_3 has to undergo relaxation to $|e\rangle$ in order to be measurable with our method. In case of a complete

nonradiative transition $|f\rangle \rightarrow \langle g|$, i. e., $\Phi_{fluo,Q_3} = 0$, pathway Q_3 will not contribute to the total signal.

Second, pathways Q_1 and Q_3 probe the same coherences of $|f\rangle\langle g|$ and $|f\rangle\langle e|$ for the 2Q and $|e\rangle\langle g|$ and $|f\rangle\langle g|$ for the 1Q-2Q case, respectively. Given the different sign of the pathways, an equal contribution of Q_1 and Q_3 will lead to their cancellation, leaving only pathway Q_2 with a negative sign. A complete signal cancellation of all pathways for equal transition energies like in the noncollinear geometry [47] is not possible, though.

Third, the 2Q contribution probes a coherence that is not probed with 1Q-2Q, namely the $|f\rangle\langle e|$ coherence. This in principle enables easier interpretation of 1Q-2Q spectra, since there are less coherences that can convolute [62]. Table 5.1 lists the possible coherences contained in 2Q and 1Q-2Q contributions.

Probed coherences	Pathway	2Q	1Q-2Q
$\|e\rangle\langle g\|$	$-Q_1$		X
	$-Q_2$	X	X
	$+Q_3$		X
$\|f\rangle\langle g\|$	$-Q_1$	X	X
	$-Q_2$	X	X
	$+Q_3$	X	X
$\|f\rangle\langle e\|$	$-Q_1$	X	
	$-Q_2$		
	$+Q_3$	X	

Table 5.1: Probed coherences for 2Q and 1Q-2Q pathways of a three-level system. In case a coherence can be probed with 2Q or 1Q-2Q, the respective pathway is marked with an X.

In order to evaluate and verify the prior conclusions, we conducted a series of simulations of an electronic three-level system, which is the simplest model that can exhibit 2Q coherences. It consists of quantum states $|g\rangle$, $|e\rangle$ and $|f\rangle$ with slightly differing transition energies of $\hbar\omega_{eg} = 2.00$ eV and of $\hbar\omega_{fe} = 2.05$ with assumed transition strengths $\gamma_{eg} = \gamma_{fe}$. The pure dephasing constants were set to $T^d_{eg} = 40$ fs and $T^d_{fg} = T^d_{fe} = 20$ fs. The simulated 2D experiment was carried out with the sampling parameters from section 5.1. As excitation sequence we applied three bandwidth-limited Gaussian pulses with a duration of 10 fs (FWHM) and a central energy of 2.05 eV each.

We simulated the 2Q and 1Q-2Q signals for indirect Q_3 fluorescence quantum yields of $\Phi_{fluo,Q_3} = 0\%$, $\Phi_{fluo,Q_3} = 50\%$, and $\Phi_{fluo,Q_3} \approx 90\%$. In accordance to Kasha's rule, we allowed only fluorescence from $|e\rangle$, with a direct quantum yield of $\Phi_{fluo,|e\rangle} = 100\%$ for simplicity. Hence, transition $|e\rangle \rightarrow \langle g|$ corresponds to fluorescence emission while transitions $|f\rangle \rightarrow \langle g|$ and $|f\rangle \rightarrow \langle e|$ are nonradiative. The fluorescence quantum

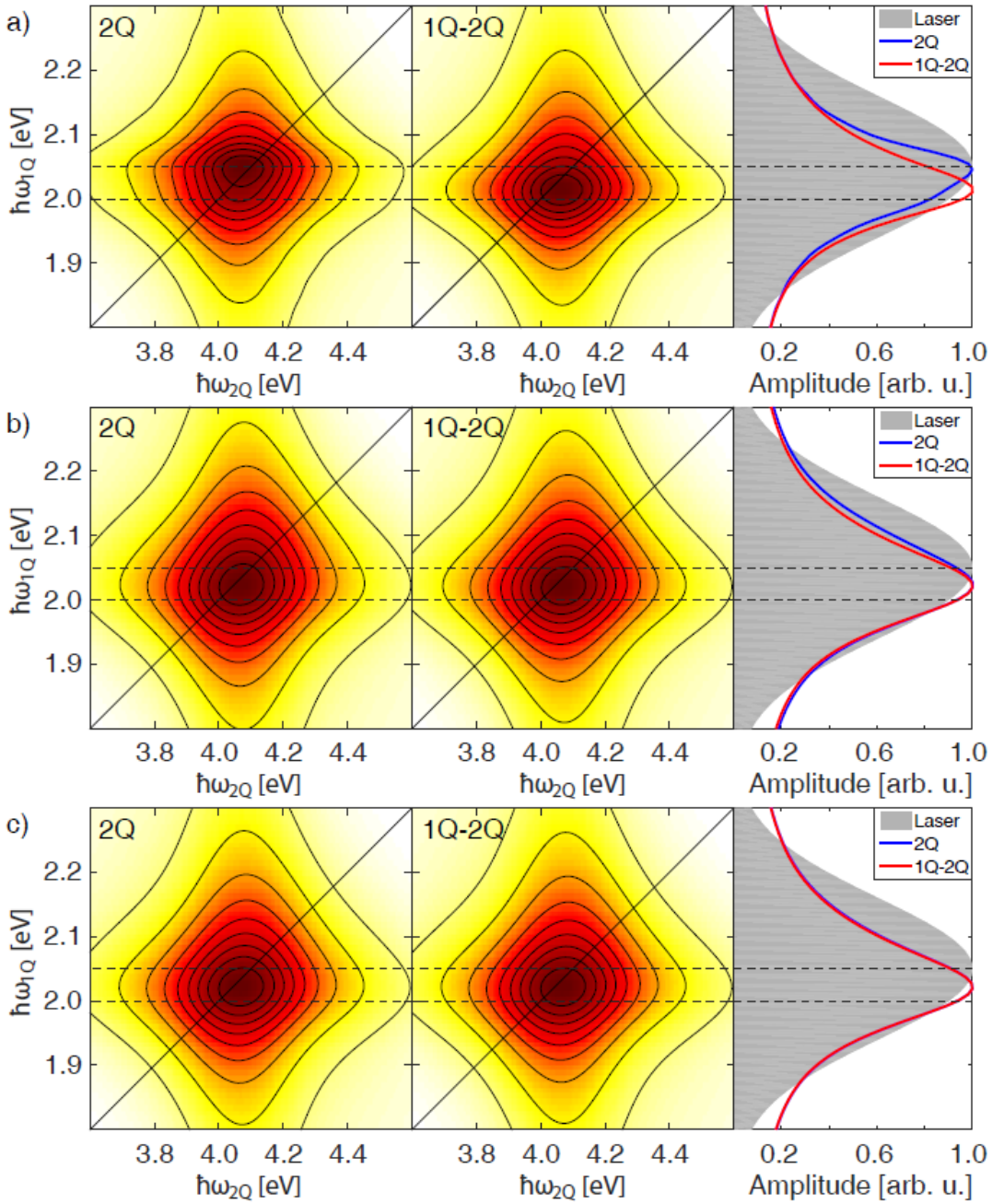

Figure 5.2: Influence of fluorescence quantum yield $\Phi_{fluo,|f\rangle}$ on absolute-valued simulated 2Q and 1Q-2Q spectra for a) $\Phi_{fluo,Q_3} = 0\%$, b) $\Phi_{fluo,Q_3} = 50\%$, and c) $\Phi_{fluo,Q_3} \approx 90\%$. For each subfigure, the right panel depicts the simulated excitation spectrum (grey) and the normalized projections along the 2Q axis of the 2Q (blue) and 1Q-2Q (red) contribution. The dashed lines indicate the transition energies $\hbar\omega_{eg}$ and $\hbar\omega_{fe}$. It is apparent that the difference in peak positions vanishes due to pathway cancellation with increasing involvement of pathway Q_3. Adopted from Supporting Information of [2].

yield of pathway Q_3 was then adjusted by varying the population-relaxation time constants for the $|f\rangle \rightarrow \langle g|$ and $|f\rangle \rightarrow \langle e|$ transitions. Allowing only the $|f\rangle \rightarrow \langle g|$ relaxation channel leads to $\Phi_{fluo,Q_3} = 0\%$. Adding a relaxation channel $|f\rangle \rightarrow \langle e|$ with the same population relaxation time constant, i. e., a ratio of 1 : 1 yields $\Phi_{fluo,Q_3} = 50\%$. Increasing the time constant of $|f\rangle \rightarrow \langle e|$ by a factor of 10 leads to a ratio of 10 : 1 and $\Phi_{fluo,Q_3} \approx 90\%$.

Figure 5.2 illustrates the results of the simulation series. With no contribution of Q_3 to the fluorescence signal, i. e., a complete nonradiative relaxation, the 2Q and 1Q-2Q signals are well distinguishable (fig. 5.2 a)). It is clearly visible that the 1Q-2Q spectrum is less congested for this case. Nevertheless, even with only half the $|f\rangle$ population relaxing nonradiatively to the ground state $|g\rangle$, the differences between 2Q and 1Q-2Q become less visible (fig. 5.2 b)), vanishing almost completely for $\Phi_{fluo,Q_3} \approx 90\%$ (fig. 5.2 c)) due to pathway cancellation.

1Q-2Q spectroscopy therefore seems to be most useful for molecular systems that exhibit high nonradiative relaxation from higher electronic states, e. g., in the presence of conical intersections in particular and for systems with a high density of states in general, that exhibit a high amount of relaxation channels. In this case multiple features are expected in a 2Q signal compared to a 1Q-2Q spectrum, potentially hindering an unambiguous interpretation.

Another detail of the simulation series worth noting is that the peak position of the projections of both 2D spectra onto the mutual 1Q domains is offset to the expected transition energy $\hbar\omega_{eg} = 2.00$ eV by ~ 0.025 eV (see right panels of fig. 5.2). We furthermore observe a tail towards higher frequencies, especially along the 1Q axes, for both the 2Q and 1Q-2Q signals, which can be attributed to finite-pulse-duration effects that have been discussed for noncollinear 2D spectroscopy [57,58]. This laser-pulling effect has to be considered when interpreting 2D spectra since it can lead to inaccurate conclusion if the exact energy detuning is not known. Reconstructing the experimental data with simulations offers the opportunity to include these effects among others and facilitates an accurate quantitative spectra interpretation.

5.2.2 Simulation parameters for modeling of experimental data

For reproduction of the experimental data, we considered an electronic three-level monomer system with ground state $|g\rangle$, singly excited state $|e\rangle$ and doubly excited state $|f\rangle$. We further assumed vibrational sublevels $|e'\rangle$ and $|f'\rangle$ and an additional sublevel $|e_{\mathrm{rel}}\rangle$, representing the excited state vibrational ground state after solvent-shell relaxation and thus the model is invoking the dynamic Stokes shift. For an illustration of the applied model system see fig. 5.1 c).

The assumption of excited-state vibrational sublevels is necessary, because organic dyes exhibit vibrational progression [98]. Furthermore, it has been shown that the vibronic structure influences the line shapes of 2Q 2D spectra [44, 47]. In contrast, the vibrationally excited ground state can be neglected since it is not involved in any

2Q Liouville pathway. Inertial solvent-shell relaxation reportedly takes place during a few tens of femtoseconds in ethanol [103–105].

We applied eq. (5.1) with the density-matrix elements $\rho = \sum_m^M \sum_n^N P_{mn} |m\rangle \langle n|$ with $m, n \in \{g, e_{\mathrm{rel}}, e, e', f, f'\}$. The energies were set to $E_g = 0$ eV, $E_{e_{\mathrm{rel}}} = 2.020$ eV, $E_e = 2.058$ eV, $E_{e'} = 2.203$ eV, $E_f = 4.237$ eV and $E_{f'} = 4.382$ eV. E_e and $E_{e'}$ had been determined from fitting the linear absorption spectrum with three Gaussian absorption peaks, of which the two main peaks were considered to be relevant for a simple modeling of the linear absorption. $E_{e_{\mathrm{rel}}}$ can be determined by E_e minus half the Stokes shift energy. The same energy spacing between $|e\rangle$ and $|e'\rangle$ was assumed for $|f\rangle$ and $|f'\rangle$, i. e. equal excited-state vibrational frequencies [47].

For determination of E_f and $E_{f'}$, a simulation series has been carried out with an initial value of $E_f = 2 \cdot E_e + \Delta$, where Δ is the correlation energy shift Δ_{exp} as obtained from the experimental data. The value of Δ was then varied in a systematic manner in order to find the best fit for the experimental data. For this purpose, the resulting simulated real parts of the 2Q and 1Q-2Q 2D spectra have been compared with the experimental data via root-mean-square deviation analysis according to eq. (4.1). The optimum result $\Delta = 121$ meV was used for further simulations, yielding the above values of E_f and $E_{f'}$.

Taking the square root of the normalized linear absorption spectrum (see fig. 5.1 a)) at $\hbar\omega_{eg} = 2.058$ eV and $\hbar\omega_{e'g} = 2.203$ eV yields $\gamma_{eg} = 1.0$ and $\gamma_{e'g} = 0.72$ as the individual relative transition strengths γ_{mn} of the interaction Hamiltonian $H_I(t')$.

For adjusting the transition strengths of the excited-state absorption $|e\rangle \rightarrow |f\rangle$ and $|e'\rangle \rightarrow |f'\rangle$, we systematically varied γ_{ef} and $\gamma_{e'f'}$ and found that the optimum reproduction quality is given for $\gamma_{ef} = 2.0$ and $\gamma_{e'f'} = 2.0$.

For the employed six-level model system, the Lindblad operators $\mathcal{L}_j^\dagger$ and $\mathcal{L}_j$ are 6×6 matrices. The dephasing processes are accounted for with $\mathcal{L}_j^{deph} = |m\rangle \langle m| + (-1) |n\rangle \langle n|$, while the population relaxations are given by $\mathcal{L}_j^{rel} = |m\rangle \langle n|$. The matrix entries in $\mathcal{L}_j^{rel}$ are all zero except the ket-bra for the desired transition, where the matrix entry is unity.

Via adjusting the time constants T_j for pure dephasing and population relaxation processes between levels it is possible to fit the peak amplitudes and line shapes of the experimental 2D spectra. The population-relaxation time constants T_{mn}^p were set to $T_{e_{\mathrm{rel}}g}^p = 3.2$ ns, which is a typical fluorescence lifetime [106], $T_{ee_{\mathrm{rel}}}^p = 10$ fs, $T_{e'e}^p = T_{f'f}^p = 100$ fs and $T_{fe}^p = T_{f'e'}^p = T_{fg}^p = T_{f'g}^p = 200$ fs. These parameters result in a Q_3 fluorescence quantum yield of $\Phi_{Q_3,fluo} = 50\%$. Pure dephasing time constants T_{mn}^d were set to $T_{eg}^d = T_{ee_{\mathrm{rel}}}^d = 10$ fs and $T_{e_{\mathrm{rel}}g}^d = T_{e'g}^d = T_{fg}^d = T_{f'g}^d = T_{e'e_{\mathrm{rel}}}^d = T_{e'e}^d = T_{fe}^d = T_{f'e'}^d = T_{f'f}^d = 80$ fs.

The simulated fluorescence signal was then obtained by calculating the integrated density matrix element $\mathbf{Tr}\{|e_{\mathrm{rel}}\rangle \langle e_{\mathrm{rel}}|\}$ after the interaction of a simulated pulse sequence that corresponded to the experimental pulse sequence, which has been described in section 5.1.

5.2.3 Influence of excitation spectrum

As shown in subsection 5.2.1, the excitation spectrum has a non-negligible influence on the 2D signal shapes. The experimental excitation spectrum shows modulation (see fig. 5.1 a), which can additionally disguise the molecular signals and complicate a correct data interpretation. In order to evaluate the influence of the spectral shape on the obtained 2D data, we performed a simulation with the actual laser spectrum and a simulation with a super-Gaussian fit of the laser spectrum and compared them with the experimental data. The simulations were carried out with the parameter set from subsection 5.2.2 and assuming a flat phase.

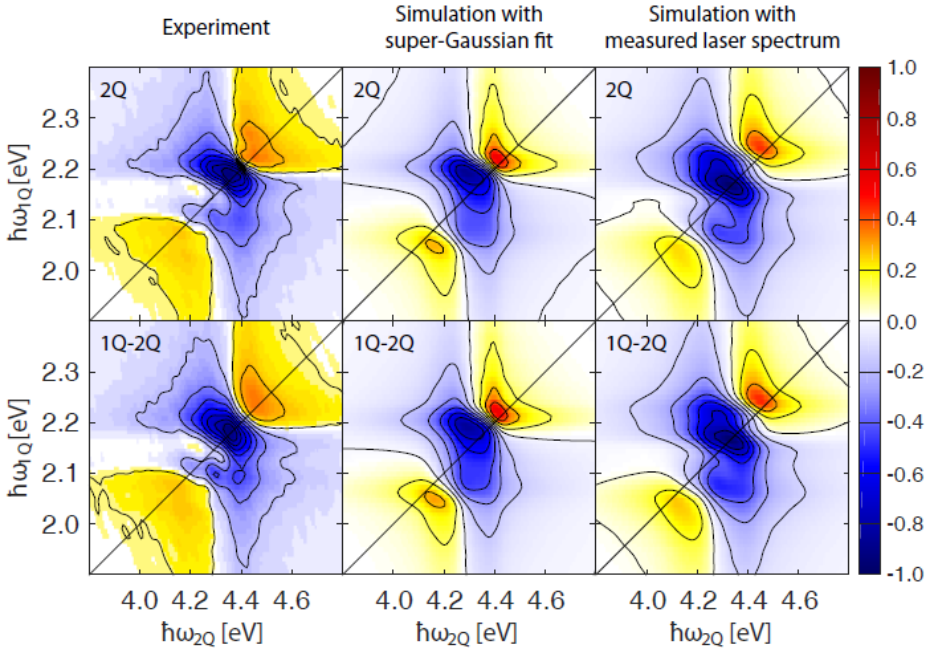

Figure 5.3: Influence of excitation spectrum on real-valued 2Q (top) and 1Q-2Q (bottom) 2D spectra. Experimental spectra (left), simulated spectra with super-Gaussian fit of the excitation spectrum (middle), simulated spectra with the measured excitation spectrum (right). Adopted from Supporting Information of [2].

Figure 5.3 illustrates the results of the comparison. The row-shaped features of the experimental data are reproduced by both simulation approaches, leading to the conclusion that they predominantly arise from molecular response and not the laser spectrum alone. However, a peak splitting of the diagonal peak is observed for the simulation with the measured laser spectrum. Since it is not present in either the experimental data or the super-Gaussian simulation, this can be attributed to uncertainties in measuring the linear excitation spectrum.

A root-mean-square-deviation analysis applying eq. (4.1) revealed that the simulation with the real laser spectrum fits the experimental data better than the simulation with a super-Gaussian fit. Therefore, the simulation results employing the measured laser spectrum are considered in the analysis section below.

5.3 Data analysis

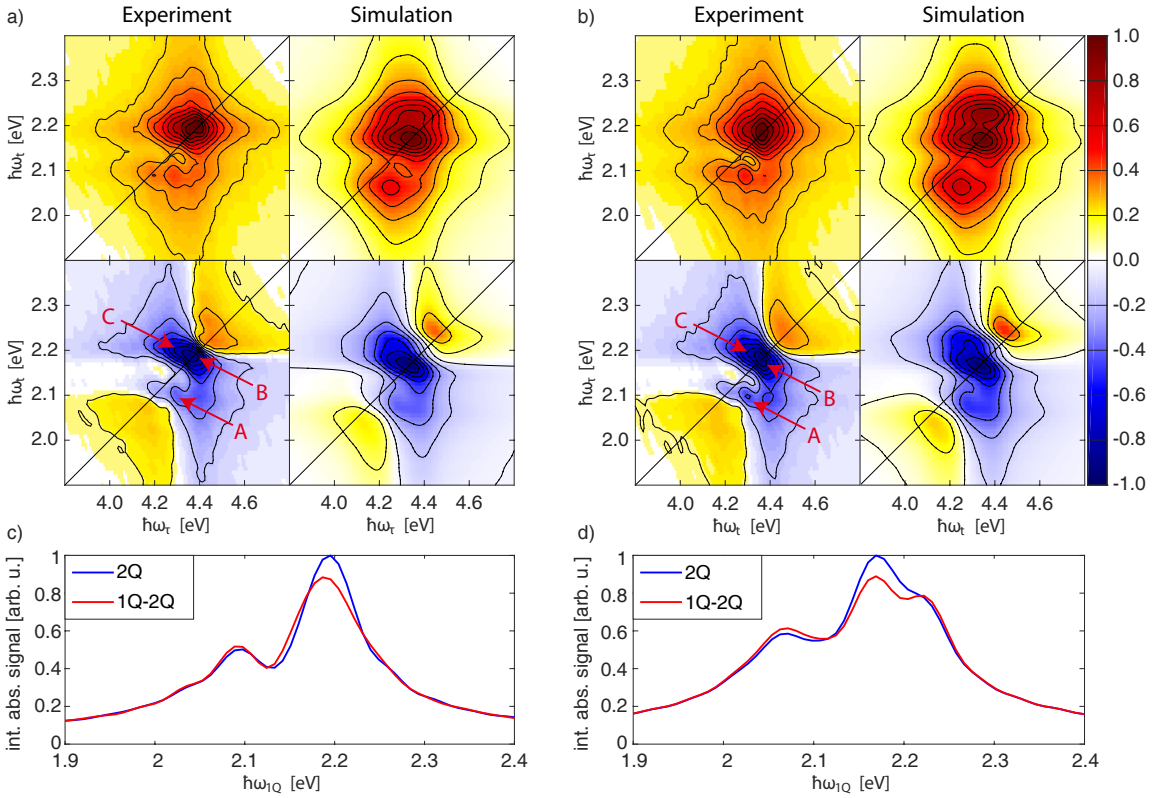

Figure 5.4: Experimental and simulated 2Q 2D (a) and 1Q-2Q (b) spectra of cresyl violet in ethanol, both shown in absolute (top) and real values (bottom), normalized to the highest absolute value of each plot. The diagonal of the spectrum is marked with a line at $\hbar\omega_\tau = 2\hbar\omega_t$ (a) and $\hbar\omega_t = 2\hbar\omega_\tau$ (b). Distinct features (A-C) are marked in the real-valued spectra. All plots are drawn with nine contour lines. (c, d) Integrated 1Q projections of 2Q and 1Q-2Q spectra (both normalized to the same absolute value) from experimental (c) and simulated (d) absolute-valued data. Adopted from [2].

The experiment was conducted following the procedure described in chapter 4 with the parameters given in section 5.1. Via eq. (2.18) the 2Q contribution was extracted

from the raw data with weighting factors $-\beta$ and $-\gamma$, and the 1Q-2Q contribution with $+\beta$ and -2γ, respectively. The rephasing 1Q contribution can also be extracted from the same data set ($+2\beta$, $-\gamma$), but is neglected in this chapter.

Figure 5.4 a) shows the absolute value (top) and real part (bottom) of experimental (left) and simulated (right) 2Q spectra. In contrast to coherence-detected 2D spectroscopy, there is no nonresonant solvent response nor any scattering contribution visible [51]. All features in the presented spectra can be attributed to molecular response that is convoluted with the employed laser spectrum, which tremendously facilitates the interpretation.

There are two row-shaped peaks visible in the absolute-valued spectrum at $\hbar\omega_t = 2.089$ eV and $\hbar\omega_t = 2.195$ eV. These signals correspond to the two vibrational sublevels of the singly excited state, $|e\rangle$ and $|e'\rangle$, that are also present in the linear absorption spectrum. The peak amplitudes, however, are inverted with respect to the expected amplitudes from the linear absorption spectrum. This may seem counterintuitive at first glance, but can be simulated by incorporating in the electronic three-level model a solvent-shell relaxation along the bath coordinate to the fluorescent state from $|e\rangle$ to $|e_{\mathrm{rel}}\rangle$ (see section 5.2.2 and fig. 5.1 b)). We employed a time constant of 10 fs for this transition. Similar time constants for solvent-shell relaxation have been reported for other molecular systems [104, 105].

The peaks are elongated along the 2Q axis $\hbar\omega_\tau$ because 2Q coherences dephase with a higher rate than 1Q coherences. As expected after inspection of the involved Liouville pathways and discussed in section 5.2.1, only negative contributions are present in the experimental and simulated real-valued spectra. The small positive features are part of the phase-twisted line shapes and thus do not represent any additional Liouville pathways [46].

The absolute value (top) and real part (bottom) of experimental (left) and simulated (right) 1Q-2Q spectra are depicted in fig. 5.4 b). For easier comparison with the 2Q spectra, the frequency axes are swapped such that the 2Q axis is represented by the x-axis in both cases.

As set out in section 5.2.1, one would expect more peaks in the 2Q spectrum than in the 1Q-2Q spectrum. This conclusion holds even more if vibrational sublevels are involved as is the case here. Nevertheless, we also showed that pathway cancellation between Q_1 and Q_3 can diminish the effect dramatically. Given the similarity between the observed 2Q and 1Q-2Q spectra, we conclude that there is indeed a high contribution of Q_3 to the overall signal due to high internal conversion efficiency from $|f\rangle$ into the fluorescent state $|e\rangle$.

An additional effect that can diminish the differentiation between 2Q and 1Q-2Q spectra is a similar energy spacing between the vibrational sublevels of the respective electronic states. Comparison of the projections of the absolute-valued contributions onto the 1Q axis of the 2Q and 1Q-2Q spectra in figures 5.4 c) and 5.4 d) reveals that peak intensity of the high-energy region is higher in the case of 2Q. We therefore assume that $\omega_{e'g} \approx \omega_{fe} \approx \omega_{f'e'}$, leaving the only distinguishable 1Q frequencies ω_{eg}

and $\omega_{e'g} \approx \omega_{fe} \approx \omega_{f'e'}$.

Peaks A and C are then assigned to 2Q frequencies ω_{fg} and peak B to $\omega_{f'g}$. The 2Q frequencies are correlated to the corresponding 1Q frequencies ω_{eg} (peak A) and $\omega_{e'g} \approx \omega_{fe} \approx \omega_{f'e'}$ (peaks B and C). Table 5.2 lists the possible 1Q and 2Q coherence combinations and provides an assignment to the observable peaks. It is apparent that the 1Q-2Q spectrum would indeed be less congested without the above mentioned effects.

		2Q axis	
		$\|f\rangle\langle g\|$	$\|f'\rangle\langle g\|$
1Q axis	$\|e\rangle\langle g\|$	A	
	$\|e'\rangle\langle g\|$	C	B
	$\|f\rangle\langle e\|$	C	B
	$\|f'\rangle\langle e'\|$	C	B

Table 5.2: 2Q and 1Q coherence contributions to peaks in the 2Q and 1Q-2Q spectra. Black letters correspond to signals that are supposed to be visible in the 2Q and 1Q-2Q spectra, red letters correspond to signals that are obtainable via 2Q only.

Determination of correlation energy

Under the assumption that peak A corresponds to pathway Q_2, we determined $\Delta_{\text{exp}} \approx \hbar\omega_{fg} - 2\hbar\omega_{eg} = 111$ meV from both 2Q and 1Q-2Q spectra, which is in fair agreement with literature on coherence-detected 2Q 2D spectroscopy (94 ± 5 meV) [44, 47]. We then used this value as a starting parameter for a simulation series where we varied Δ and compared the results with the experimental spectra as discussed in section 5.2.2. This approach accounts for uncertainties caused by finite-pulse-duration effects [57, 58] and by profile modulations of the excitation spectrum (see section 5.2.3). The optimum value was determined to be $\Delta = 121$ meV.

5.4 Summary

We performed the first experimental fluorescence-detected 2Q 2D experiment and the first experimental obtaining of the theoretically predicted 1Q-2Q contribution. The presented method circumvents the issue of nonresonant solvent response and scattering, which are inherent in coherence-detected 2Q 2D spectroscopy, by the use of fluorescence as observable. By employing phase cycling, no additional phasing procedure is needed that eventually complicates the data interpretation in the common nonlinear geometry. We applied the method to the well-investigated laser dye cresyl violet in ethanol and compared the results with simulations of a simple six-level system. The combination of experiment and systematic simulations enabled us

to estimate the time constant of solvent-shell relaxation and to determine an optimum value of the correlation energy $\Delta = 121$ meV, which is in fair agreement with literature (94 ± 5 meV) [44, 47]. Furthermore, we discussed the effects of pathway cancellation and concluded, that 1Q-2Q 2D spectroscopy will potentially facilitate quantitative analysis for molecular systems that exhibit a strong nonradiative relaxation from higher electronic states. The method has been successfully applied to other molecular systems, e. g. Rhodamine 700 [3].

6 Summary

In the last two decades, coherent multidimensional femtosecond spectroscopy has become a powerful and versatile tool to investigate chemical dynamics of a broad variety of quantum systems. The combination of transient information, equivalent to pump-probe spectroscopy, with information about coupling between energetic states and the system environment allows an extensive insight into atomic and molecular properties. Many experimental 2D setups employ the coherence-detected approach, where nonlinear system responses are emitted as coherent electric fields which are detected after spatial separation from the excitation pulses. As an alternative to this experimentally demanding approach, population-based 2D spectroscopy has been established. Here, the coherent information is encoded in the phases of a collinear excitation-pulse train and extracted from incoherent signals like fluorescence via phase cycling. In principle, the use of fluorescence as observable can boost the sensitivity down to the single-molecule level.

The aim of this work was the realization of a pulse-shaper assisted fully collinear fluorescence-detected 2D setup and the conducting of proof-of-principle experiments in the liquid phase. This inherently phase-stable and compact setup has been presented in chapter 3, with the utilized pulse shaper granting amplitude and phase modulation on a shot-to-shot basis. Two different types of white-light sources have been applied and evaluated with regard to their respective advantages for 2D fluorescence spectroscopy. A variety of artifact sources that can occur with the present setup have been discussed, and correction schemes and instructions for avoiding these artifacts have been provided.

In chapter 4, the setup has been demonstrated by employing a four-pulse sequence on cresyl violet in ethanol. A detailed data-acquisition and data-analysis procedure has been presented, where phase cycling is used for extraction of the nonlinear contributions. Depending on the phase-cycling scheme, it is possible to recover all nonlinear contributions in a single measurement. Well-known quantum-beating behavior of cresyl violet during the population time could be reproduced. Due to measuring in a rotating-frame environment and 1 kHz shot-to-shot pulse incrementation, it was possible to obtain a 2D spectrum for one population time in 6 s. Via error evaluation it has been shown that 10× averaging (1 min) is sufficient to obtain a root-mean-square error of < 0.05 compared to 400× averaging, proving that the utilized acquisition scheme is well suited.

The realization of the first experimental fluorescence-detected 2Q 2D experiment and the first experimental access to the theoretically predicted 1Q-2Q contribution

have been presented in chapter 5. For that purpose, a three-pulse sequence has been employed on cresyl violet in ethanol, and the experimental results have been compared with simulations of a simple six-level system. In contrast to coherence-detected 2Q 2D spectroscopy, no nonresonant solvent response and scattering contributions are visible with the presented setup and no additional phasing procedure is needed. Via a combination of experiment and systematic simulations, information about solvent-shell relaxation and the correlation energy were gained. On the basis of simulations, pathway cancellation effects have been discussed, concluding that 1Q-2Q 2D spectroscopy will potentially facilitate quantitative analysis for molecular systems that exhibit a strong nonradiative relaxation from higher electronic states.

Summarizing, with the presented method it is possible to acquire all nonlinear contributions with rapid data acquisition and a setup that is easy to align. The demonstrated proof-of-principle experiments constitute an extension of the 2D spectroscopic tool palette, and provide a profound basis for future applications like multidimensional spectroscopy, multi-color 2D spectroscopy or the combination of simultaneous liquid and gas-phase 2D experiments.

7 Zusammenfassung

In den letzten zwei Jahrzehnten hat sich die kohärente mehrdimensionale Femtosekunden-Spektroskopie zu einem leistungsstarken und vielseitigen Instrument zur Untersuchung der chemischen Dynamik einer Vielzahl von Quantensystemen entwickelt. Die Kombination von transienten Informationen, die der Anrege-Abrage-Spektroskopie entsprechen, mit Informationen zur Kopplung zwischen energetischen Zuständen und der Systemumgebung ermöglicht einen umfassenden Einblick in atomare und molekulare Eigenschaften. Viele experimentelle 2D-Aufbauten verwenden den kohä-renzdetektierten Ansatz, bei dem nichtlineare Systemantworten als kohärente elektrische Felder emittiert und rumlich getrennt von den Anregungspulsen detektiert werden. Als Alternative zu diesem experimentell anspruchsvollen Ansatz wurde die populationsbasierte 2D-Spektroskopie etabliert. Hier wird die kohärente Information in den Phasen einer kollinearen Anregungspulsfolge codiert und aus inkohärenten Signalen wie Fluoreszenz über *Phase Cycling* extrahiert. Grundsätzlich kann durch die Verwendung von Fluoreszenz als Observable eine Sensitivität bis zum Einzelmolekülniveau erreicht werden.

Ziel dieser Arbeit war die Realisierung eines pulsformergestützten vollständig kollinearen fluoreszenzdetektierten 2D-Aufbaus und die Durchführung von *Proof-of-Principle*-Experimenten in der Flüssigphase. Dieser inhärent phasenstabile und kompakte Aufbau wurde in Kapitel 3 vorgestellt. Der verwendete Pulsformer ermöglicht eine Amplituden- und Phasenmodulation von Schuss zu Schuss. Zwei verschiedene Arten von Weilichtquellen wurden angewendet und hinsichtlich ihrer jeweiligen Vorteile für die 2D-Fluoreszenzspektroskopie bewertet. Eine Vielzahl von Artefaktquellen, die mit dem vorliegenden Aufbau auftreten können, wurden diskutiert und Korrekturschemata und Anweisungen zur Vermeidung dieser Artefakte bereitgestellt.

In Kapitel 4 wurde der Aufbau anhand einer Vierpulssequenz mit Cresylviolett in Ethanol demonstriert. Es wurde ein detailliertes Datenerfassungs- und Datenanalyseverfahren vorgestellt, bei dem *Phase Cycling* zur Extraktion der nichtlinearen Beiträge verwendet wird. Abhängig vom *Phase Cycling*-Schema ist es möglich, alle nichtlinearen Beiträge in einer einzigen Messung aufzudecken. Literaturbekannte Oszillationen von Cresylviolett während der Populationszeit konnten reproduziert werden. Aufgrund der Messung in einer Umgebung im *Rotating Frame* und einer 1 kHz Schuss-zu-Schuss Pulsinkrementierung war es möglich, ein 2D-Spektrum für eine Populationszeit in 6 s zu erhalten. Eine Fehlerevaluierung hat gezeigt, dass eine zehnfache Mittelwertbildung (1 min) ausreicht, um eine mittlere quadratische Abweichung von < 0.05 gegenüber einer 400-fachen Mittelwertbildung zu erhalten, was

beweist, dass das verwendete Messschema gut geeignet ist.

Die Realisierung des ersten experimentellen fluoreszenzdetektierten 2Q-2D-Experiments und der erste experimentelle Zugang zum theoretisch vorhergesagten 1Q-2Q-Beitrag wurden in Kapitel 5 vorgestellt. Zu diesem Zweck wurde eine Dreipulssequenz auf Cresylviolett in Ethanol angewendet und die experimentellen Ergebnisse wurden mit Simulationen eines einfachen Sechs-Level-Systems verglichen. Im Gegensatz zur kohärenzdetektierten 2Q-2D-Spektroskopie sind bei dem vorgestellten Aufbau keine nichtresonanten Lösungsmittelsignale und Streuungsbeiträge sichtbar und es ist kein zusätzliches *Phasing*-Verfahren erforderlich. Durch eine Kombination aus Experimenten und systematischen Simulationen wurden Informationen über die Relaxation der Lösungsmittelhülle und die Korrelationsenergie gewonnen. Auf der Basis von Simulationen wurden Effekte der Pfadauslöschung diskutiert, die darauf schlieen lassen, dass die 1Q-2Q-2D-Spektroskopie möglicherweise die quantitative Analyse für molekulare Systeme erleichtert, die eine starke nichtstrahlende Relaxation aus höheren elektronischen Zuständen aufweisen.

Zusammenfassend ist es mit der vorgestellten Methode möglich, alle nichtlinearen Beiträge mit einer schnellen Datenaufnahme und einem einfach einzurichtenden Aufbau zu erfassen. Die gezeigten *Proof-of-Principle*-Experimente stellen eine Erweiterung der 2D-Spektroskopie-Werkzeugpalette dar und bieten eine fundierte Grundlage für zukünftige Anwendungen wie mehrdimensionale Spektroskopie, mehrfarbige 2D-Spektroskopie oder die Kombination von simultanen Flüssig- und Gasphasen-2D-Experimenten.

Bibliography

[1] S. Draeger, S. Roeding, and T. Brixner, "Rapid-scan coherent 2D fluorescence spectroscopy," *Optics Express*, vol. 25, pp. 3259–3267, Feb. 2017.

[2] S. Mueller, S. Draeger, X. Ma, M. Hensen, T. Kenneweg, W. Pfeiffer, and T. Brixner, "Fluorescence-detected two-quantum and one-quantum-two-quantum 2D electronic spectroscopy," *The Journal of Physical Chemistry Letters*, pp. 1964–1969, Apr. 2018.

[3] S. Mueller, S. Draeger, N. Klosterhalfen, and T. Brixner, "Fluorescence-detected two-quantum and one-quantum-two-quantum 2D electronic spectroscopy of rhodamine 700," *EPJ Web Conf.*, vol. 205, p. 03012, 2019.

[4] A. H. Zewail, "Femtochemistry. Past, present, and future," *Pure and Applied Chemistry*, vol. 72, pp. 2219–2231, July 2000. 00041.

[5] D. M. Jonas, "Two-dimensional femtosecond spectroscopy," *Annual Review of Physical Chemistry*, vol. 54, pp. 425–463, 2003.

[6] J. P. Ogilvie and K. J. Kubarych, "Chapter 5 Multidimensional Electronic and Vibrational Spectroscopy," in *Advances In Atomic, Molecular, and Optical Physics*, vol. 57, pp. 249–321, Elsevier, 2009.

[7] S. T. Cundiff and S. Mukamel, "Optical multidimensional coherent spectroscopy," *Physics Today*, vol. 66, pp. 44–49, June 2013.

[8] M. Cho, *Two-dimensional optical spectroscopy*. Boca Raton, FL: CRC Press, June 2009.

[9] T. Brixner, J. Stenger, H. M. Vaswani, M. Cho, R. E. Blankenship, and G. R. Fleming, "Two-dimensional spectroscopy of electronic couplings in photosynthesis," *Nature*, vol. 434, pp. 625–628, Mar. 2005.

[10] P. Hamm, M. Lim, W. F. DeGrado, and R. M. Hochstrasser, "The two-dimensional IR nonlinear spectroscopy of a cyclic penta-peptide in relation to its three-dimensional structure," *Proceedings of the National Academy of Sciences*, vol. 96, pp. 2036–2041, Feb. 1999.

[11] C. Consani, G. Auböck, F. v. Mourik, and M. Chergui, "Ultrafast tryptophan-to-heme electron transfer in myoglobins revealed by UV 2D spectroscopy," *Science*, vol. 339, pp. 1586–1589, Mar. 2013.

[12] N. H. C. Lewis and G. R. Fleming, "Two-dimensional electronic-vibrational spectroscopy of chlorophyll *a* and *b*," *The Journal of Physical Chemistry Letters*, vol. 7, pp. 831–837, Mar. 2016.

[13] A. Ghosh, J. S. Ostrander, and M. T. Zanni, "Watching proteins wiggle: Mapping structures with two-dimensional infrared spectroscopy," *Chemical Reviews*, Jan. 2017.

[14] P. Akhtar, C. Zhang, T. N. Do, G. Garab, P. H. Lambrev, and H.-S. Tan, "Two-dimensional spectroscopy of chlorophyll *a* excited-state equilibration in light-harvesting complex II," *The Journal of Physical Chemistry Letters*, vol. 8, pp. 257–263, Jan. 2017.

[15] S. Ruetzel, M. Diekmann, P. Nuernberger, C. Walter, B. Engels, and T. Brixner, "Multidimensional spectroscopy of photoreactivity," *Proceedings of the National Academy of Sciences*, vol. 111, pp. 4764–4769, Jan. 2014.

[16] R. D. Mehlenbacher, T. J. McDonough, M. Grechko, M.-Y. Wu, M. S. Arnold, and M. T. Zanni, "Energy transfer pathways in semiconducting carbon nanotubes revealed using two-dimensional white-light spectroscopy," *Nature Communications*, vol. 6, p. 6732, Apr. 2015.

[17] K. W. Stone, K. Gundogdu, D. B. Turner, X. Li, S. T. Cundiff, and K. A. Nelson, "Two-quantum 2D FT electronic spectroscopy of biexcitons in GaAs quantum wells," *Science*, vol. 324, pp. 1169–1173, May 2009.

[18] L. M. Kiefer and K. J. Kubarych, "Solvent-dependent dynamics of a series of rhenium photoactivated catalysts measured with ultrafast 2DIR," *The Journal of Physical Chemistry A*, vol. 119, pp. 959–965, Feb. 2015.

[19] W. P. Aue, E. Bartholdi, and R. R. Ernst, "Two-dimensional spectroscopy. Application to nuclear magnetic resonance," *The Journal of Chemical Physics*, vol. 64, no. 5, pp. 2229–2246, 1976.

[20] Y. Tanimura and S. Mukamel, "Two-dimensional femtosecond vibrational spectroscopy of liquids," *The Journal of Chemical Physics*, vol. 99, pp. 9496–9511, Dec. 1993.

[21] S. Mukamel, *Principles of nonlinear optical spectroscopy*. New York: Oxford University Press, 1st ed., 1995.

[22] L. Lepetit and M. Joffre, "Two-dimensional nonlinear optics using Fourier-transform spectral interferometry," *Optics Letters*, vol. 21, pp. 564–566, Apr. 1996.

[23] C.-H. Tseng, S. Matsika, and T. C. Weinacht, "Two-dimensional ultrafast Fourier transform spectroscopy in the deep ultraviolet," *Optics Express*, vol. 17, pp. 18788–18793, Oct. 2009.

[24] U. Selig, C.-F. Schleussner, M. Foerster, F. Langhojer, P. Nuernberger, and T. Brixner, "Coherent two-dimensional ultraviolet spectroscopy in fully noncollinear geometry," *Optics Letters*, vol. 35, pp. 4178–4180, Dec. 2010.

[25] M. L. Cowan, J. P. Ogilvie, and R. J. D. Miller, "Two-dimensional spectroscopy using diffractive optics based phased-locked photon echoes," *Chemical Physics Letters*, vol. 386, pp. 184–189, Mar. 2004.

[26] T. Brixner, I. V. Stiopkin, and G. R. Fleming, "Tunable two-dimensional femtosecond spectroscopy," *Optics Letters*, vol. 29, pp. 884–886, Apr. 2004.

[27] U. Selig, F. Langhojer, F. Dimler, T. Lhrig, C. Schwarz, B. Gieseking, and T. Brixner, "Inherently phase-stable coherent two-dimensional spectroscopy using only conventional optics," *Optics Letters*, vol. 33, no. 23, pp. 2851–2853, 2008.

[28] J. D. Hybl, A. W. Albrecht, S. M. Gallagher Faeder, and D. M. Jonas, "Two-dimensional electronic spectroscopy," *Chemical Physics Letters*, vol. 297, pp. 307–313, Nov. 1998.

[29] P. Hamm, M. Lim, and R. M. Hochstrasser, "Structure of the amide I band of peptides measured by femtosecond nonlinear-infrared spectroscopy," *The Journal of Physical Chemistry B*, vol. 102, pp. 6123–6138, July 1998.

[30] M. Woerner, W. Kuehn, P. Bowlan, K. Reimann, and T. Elsaesser, "Ultrafast two-dimensional terahertz spectroscopy of elementary excitations in solids," *New Journal of Physics*, vol. 15, p. 025039, Feb. 2013.

[31] P. Tian, D. Keusters, Y. Suzaki, and W. S. Warren, "Femtosecond phase-coherent two-dimensional spectroscopy," *Science*, vol. 300, pp. 1553–1555, June 2003.

[32] P. F. Tekavec, G. A. Lott, and A. H. Marcus, "Fluorescence-detected two-dimensional electronic coherence spectroscopy by acousto-optic phase modulation," *The Journal of Chemical Physics*, vol. 127, p. 214307, Dec. 2007.

[33] G. A. Lott, A. Perdomo-Ortiz, J. K. Utterback, J. R. Widom, A. Aspuru-Guzik, and A. H. Marcus, "Conformation of self-assembled porphyrin dimers in liposome vesicles by phase-modulation 2D fluorescence spectroscopy," *Proceedings of the National Academy of Sciences*, vol. 108, pp. 16521–16526, Oct. 2011.

[34] A. Perdomo-Ortiz, J. R. Widom, G. A. Lott, A. Aspuru-Guzik, and A. H. Marcus, "Conformation and electronic population transfer in membrane-supported self-assembled porphyrin dimers by 2D fluorescence spectroscopy," *The Journal of Physical Chemistry B*, vol. 116, pp. 10757–10770, Sept. 2012.

[35] J. R. Widom, N. P. Johnson, P. H. v. Hippel, and A. H. Marcus, "Solution conformation of 2-aminopurine dinucleotide determined by ultraviolet two-dimensional fluorescence spectroscopy," *New Journal of Physics*, vol. 15, p. 025028, Feb. 2013.

[36] J. R. Widom, W. Lee, A. Perdomo-Ortiz, D. Rappoport, T. F. Molinski, A. Aspuru-Guzik, and A. H. Marcus, "Temperature-dependent conformations of a membrane supported zinc porphyrin tweezer by 2D fluorescence spectroscopy," *The Journal of Physical Chemistry A*, Mar. 2013.

[37] A. K. De, D. Monahan, J. M. Dawlaty, and G. R. Fleming, "Two-dimensional fluorescence-detected coherent spectroscopy with absolute phasing by confocal imaging of a dynamic grating and 27-step phase-cycling," *The Journal of Chemical Physics*, vol. 140, p. 194201, May 2014.

[38] M. Aeschlimann, T. Brixner, A. Fischer, C. Kramer, P. Melchior, W. Pfeiffer, C. Schneider, C. Strüber, P. Tuchscherer, and D. V. Voronine, "Coherent two-dimensional nanoscopy," *Science*, vol. 333, pp. 1723–1726, Sept. 2011.

[39] G. Nardin, T. M. Autry, K. L. Silverman, and S. T. Cundiff, "Multidimensional coherent photocurrent spectroscopy of a semiconductor nanostructure," *Optics Express*, vol. 21, pp. 28617–28627, Nov. 2013.

[40] K. J. Karki, J. R. Widom, J. Seibt, I. Moody, M. C. Lonergan, T. Pullerits, and A. H. Marcus, "Coherent two-dimensional photocurrent spectroscopy in a PbS quantum dot photocell," *Nature Communications*, vol. 5, p. 5869, Dec. 2014.

[41] S. Roeding and T. Brixner, "Molecular-beam coherent 2D electronic spectroscopy reveals ionization pathways," *Submitted for publication.*, 2017.

[42] P. Malý and T. Mančal, "Signatures of exciton delocalization and exciton-exciton annihilation in fluorescence-detected two-dimensional coherent spectroscopy," *The Journal of Physical Chemistry Letters*, vol. 9, no. 19, pp. 5654–5659, 2018. PMID: 30188728.

[43] E. C. Fulmer, P. Mukherjee, A. T. Krummel, and M. T. Zanni, "A pulse sequence for directly measuring the anharmonicities of coupled vibrations: Two-quantum two-dimensional infrared spectroscopy," *The Journal of Chemical Physics*, vol. 120, pp. 8067–8078, May 2004.

[44] J. Kim, S. Mukamel, and G. D. Scholes, "Two-dimensional electronic double-quantum coherence spectroscopy," *Accounts of Chemical Research*, vol. 42, pp. 1375–1384, Sept. 2009.

[45] A. Nemeth, J. Sperling, J. Hauer, H. F. Kauffmann, and F. Milota, "Compact phase-stable design for single- and double-quantum two-dimensional electronic spectroscopy," *Optics Letters*, vol. 34, pp. 3301–3303, Nov. 2009.

[46] A. Nemeth, F. Milota, T. Manal, T. Pullerits, J. Sperling, J. Hauer, H. F. Kauffmann, and N. Christensson, "Double-quantum two-dimensional electronic spectroscopy of a three-level system: Experiments and simulations," *The Journal of Chemical Physics*, vol. 133, p. 094505, Sept. 2010.

[47] J. Kim, V. M. Huxter, C. Curutchet, and G. D. Scholes, "Measurement of electron-electron interactions and correlations using two-dimensional electronic double-quantum coherence spectroscopy," *The Journal of Physical Chemistry A*, vol. 113, pp. 12122–12133, Nov. 2009.

[48] K. W. Stone, D. B. Turner, K. Gundogdu, S. T. Cundiff, and K. A. Nelson, "Exciton-exciton correlations revealed by two-quantum, two-dimensional Fourier transform optical spectroscopy," *Accounts of Chemical Research*, vol. 42, pp. 1452–1461, Sept. 2009.

[49] N. Christensson, F. Milota, A. Nemeth, I. Pugliesi, E. Riedle, J. Sperling, T. Pullerits, H. F. Kauffmann, and J. Hauer, "Electronic double-quantum coherences and their impact on ultrafast spectroscopy: The example of β-Carotene," *The Journal of Physical Chemistry Letters*, vol. 1, pp. 3366–3370, Dec. 2010.

[50] P. E. Konold and R. Jimenez, "Excited State Electronic Landscape of mPlum Revealed by Two-Dimensional Double Quantum Coherence Spectroscopy," *The Journal of Physical Chemistry B*, vol. 119, pp. 3414–3422, Feb. 2015.

[51] T. A. Gellen, L. A. Bizimana, W. P. Carbery, I. Breen, and D. B. Turner, "Ultrabroadband two-quantum two-dimensional electronic spectroscopy," *The Journal of Chemical Physics*, vol. 145, p. 064201, Aug. 2016.

[52] J. P. Ogilvie and K. J. Kubarych, "Multidimensional electronic and vibrational spectroscopy: An ultrafast probe of molecular relaxation and reaction dynamics," in *Advances In Atomic, Molecular, and Optical Physics*, vol. 57, pp. 249–321, Academic Press, 2009.

[53] P. Hamm and M. Zanni, *Concepts and methods of 2D infrared spectroscopy*. New York: Cambridge University Press, 1 ed., Feb. 2011.

[54] J. Dostál, F. Fennel, F. Koch, S. Herbst, F. Würthner, and T. Brixner, "Direct observation of exciton-exciton interactions," *Nature Communications*, vol. 9, Dec. 2018.

[55] J. Süss, J. Wehner, J. Dostäl, T. Brixner, and V. Engel, "Mapping of exciton-exciton annihilation in a molecular dimer via fifth-order femtosecond two-dimensional spectroscopy," *The Journal of Chemical Physics*, vol. 150, p. 104304, Mar. 2019.

[56] T. Brixner, *Coherent Multidimensional Spectroscopy and Quantum Control*. Habilitationsschrift, Würzburg, 2005.

[57] C. L. Smallwood, T. M. Autry, and S. T. Cundiff, "Analytical solutions to the finite-pulse Bloch model for multidimensional coherent spectroscopy," *JOSA B*, vol. 34, pp. 419–429, Feb. 2017.

[58] V. Perlk, J. Hauer, and F. anda, "Finite pulse effects in single and double quantum spectroscopies," *JOSA B*, vol. 34, pp. 430–439, Feb. 2017.

[59] S. Mukamel, R. Oszwadowski, and L. Yang, "A coherent nonlinear optical signal induced by electron correlations," *The Journal of Chemical Physics*, vol. 127, p. 221105, Dec. 2007.

[60] T. Brixner and G. Gerber, "Adaptive quantum control of femtochemistry," *Physica Scripta*, vol. 110, p. 101, 2004.

[61] W. Wagner, C. Li, J. Semmlow, and W. Warren, "Rapid phase-cycled two-dimensional optical spectroscopy in fluorescence and transmission mode," *Optics Express*, vol. 13, pp. 3697–3706, May 2005.

[62] H.-S. Tan, "Theory and phase-cycling scheme selection principles of collinear phase coherent multi-dimensional optical spectroscopy," *The Journal of Chemical Physics*, vol. 129, p. 124501, Sept. 2008.

[63] R. P. Feynman, "Space-time approach to quantum electrodynamics," *Physical Review*, vol. 76, no. 6, p. 769, 1949.

[64] T. K. Yee and T. K. Gustafson, "Diagrammatic analysis of the density operator for nonlinear optical calculations: Pulsed and cw responses," *Physical Review A*, vol. 18, pp. 1597–1617, Oct. 1978.

[65] S. A. J. Druet and J.-P. E. Taran, "Cars spectroscopy," *Progress in Quantum Electronics*, vol. 7, pp. 1–72, Jan. 1981.

[66] M. Kasha, "Characterization of electronic transitions in complex molecules," *Discussions of the Faraday Society*, vol. 9, p. 14, 1950.

[67] J.-C. Diels and W. Rudolph, *Ultrashort Laser Pulse Phenomena: Fundamentals, Techniques, and Applications on a Femtosecond Time Scale (Optics and Photonics Series)*. Academic Press Inc., 2nd ed., 2006.

[68] R. W. Boyd, *Nonlinear optics*. Burlington: Academic Press, 3rd ed., Apr. 2008.

[69] J.-C. Diels and W. Rudolph, *Ultrashort laser pulse phenomena: Fundamentals, techniques, and applications on a femtosecond time scale*. Academic Press Inc, 2nd ed., May 1996.

[70] E. Riedle, M. Beutter, S. Lochbrunner, J. Piel, S. Schenkl, S. Sporlein, and W. Zinth, "Generation of 10 to 50 fs pulses tunable through all of the visible and the NIR," *Applied Physics B: Lasers and Optics*, vol. 71, pp. 457–465, Sept. 2000.

[71] G. Cerullo and S. De Silvestri, "Ultrafast optical parametric amplifiers," *Review of Scientific Instruments*, vol. 74, pp. 1–18, Jan. 2003.

[72] F. D. Fuller and J. P. Ogilvie, "Experimental implementations of two-dimensional Fourier transform electronic spectroscopy," *Annual Review of Physical Chemistry*, vol. 66, no. 1, pp. 667–690, 2015.

[73] L. Conversion, "Topas Series Traveling-wave Optical Parametric Amplifiers, User's Manual," 2009.

[74] X. Ma, J. Dostál, and T. Brixner, "Broadband 7-fs diffractive-optic-based 2D electronic spectroscopy using hollow-core fiber compression," *Optics Express*, vol. 24, pp. 20781–20791, Sept. 2016.

[75] M. Wollenhaupt, A. Assion, and T. Baumert, *Springer Handbook of Lasers and Optics*. New York: Springer Science+Business Media, 2007.

[76] S. Akturk, X. Gu, M. Kimmel, and R. Trebino, "Extremely simple single-prism ultrashort-pulse compressor," *Optics Express*, vol. 14, pp. 10101–10108, Oct. 2006.

[77] Fastlite, "DAZZLER TM WR-510-950 Specifications," tech. rep., Mar. 2016.

[78] R. Trebino, K. W. DeLong, D. N. Fittinghoff, J. N. Sweetser, M. A. Krumbügel, and B. A. Richman, "Measuring ultrashort laser pulses in the time-frequency domain using frequency-resolved optical gating," *Review of Scientific Instruments*, vol. 68, pp. 3277–3295, 1997.

[79] A. Galler and T. Feurer, "Pulse shaper assisted short laser pulse characterization," *Applied Physics B: Lasers and Optics*, vol. 90, pp. 427–430, Mar. 2008.

[80] A. Monmayrant, S. Weber, and B. Chatel, "A newcomer's guide to ultrashort pulse shaping and characterization," *Journal of Physics B: Atomic, Molecular and Optical Physics*, vol. 43, p. 103001, May 2010.

[81] P. Nuernberger, G. Vogt, T. Brixner, and G. Gerber, "Femtosecond quantum control of molecular dynamics in the condensed phase," *Physical Chemistry Chemical Physics*, vol. 9, no. 20, pp. 2470–2497, 2007.

[82] P. Tournois, "Acousto-optic programmable dispersive filter for adaptive compensation of group delay time dispersion in laser systems," *Optics Communications*, vol. 140, pp. 245–249, Aug. 1997.

[83] S. Roeding, *Coherent Multidimensional Spectroscopy in Molecular Beams and Liquids Using Incoherent Observables*. PhD thesis, Würzburg, 2017.

[84] N. Krebs, R. A. Probst, and E. Riedle, "Sub-20 fs pulses shaped directly in the UV by an acousto-optic programmable dispersive filter," *Optics Express*, vol. 18, pp. 6164–6171, Mar. 2010.

[85] D. J. McCabe, D. R. Austin, A. Tajalli, S. Weber, I. A. Walmsley, and B. Chatel, "Space-time coupling of shaped ultrafast ultraviolet pulses from an acousto-optic programmable dispersive filter," *Journal of the Optical Society of America B*, vol. 28, pp. 58–64, Jan. 2011.

[86] N. M. Kearns, R. D. Mehlenbacher, A. C. Jones, and M. T. Zanni, "Broadband 2D electronic spectrometer using white light and pulse shaping: noise and signal evaluation at 1 and 100 kHz," *Optics Express*, vol. 25, pp. 7869–7883, Apr. 2017.

[87] C. E. Shannon, "Communication in the presence of noise," *Proceedings of the IRE*, vol. 37, pp. 10–21, Jan. 1949.

[88] H. Nyquist, "Certain topics in telegraph transmission theory," *Transactions of the American Institute of Electrical Engineers*, vol. 47, pp. 617–644, Apr. 1928.

[89] F. Kanal, S. Keiber, R. Eck, and T. Brixner, "100-kHz shot-to-shot broadband data acquisition for high-repetition-rate pump-probe spectroscopy," *Optics Express*, vol. 22, pp. 16965–16975, July 2014.

[90] P. Tyagi, J. I. Saari, B. Walsh, A. Kabir, V. Crozatier, N. Forget, and P. Kambhampati, "Two-color two-dimensional electronic spectroscopy using dual acousto-optic pulse shapers for complete amplitude, phase, and polarization control of femtosecond laser pulses," *The Journal of Physical Chemistry A*, vol. 117, pp. 6264–6269, July 2013.

[91] H. Seiler, B. Walsh, S. Palato, A. Thai, V. Crozatier, N. Forget, and P. Kambhampati, "Kilohertz generation of high contrast polarization states for visible femtosecond pulses via phase-locked acousto-optic pulse shapers," *Journal of Applied Physics*, vol. 118, p. 103110, Sept. 2015.

[92] C. Schwarz, O. Hüter, and T. Brixner, "Full vector-field control of ultrashort laser pulses utilizing a single dual-layer spatial light modulator in a common-path setup," *Journal of the Optical Society of America B: Optical Physics*, vol. 32, pp. 933–945, May 2015.

[93] S. Ruetzel, C. Stolzenberger, F. Dimler, D. J. Tannor, and T. Brixner, "Adaptive coherent control using the von Neumann basis," *Physical Chemistry Chemical Physics*, vol. 13, no. 19, pp. 8627–8636, 2011.

[94] G. Otting, H. Widmer, G. Wagner, and K. Wüthrich, "Origin of $\tau 2$ and $\tau 2$ ridges in 2D NMR spectra and procedures for suppression," *Journal of Magnetic Resonance (1969)*, vol. 66, pp. 187–193, Jan. 1986.

[95] S. Goetz, D. Li, V. Kolb, J. Pflaum, and T. Brixner, "Coherent two-dimensional fluorescence micro-spectroscopy," *Optics Express*, vol. 26, pp. 3915–3925, Feb. 2018.

[96] S. J. Isak and E. M. Eyring, "Fluorescence quantum yield of cresyl violet in methanol and water as a function of concentration," *The Journal of Physical Chemistry*, vol. 96, pp. 1738–1742, Feb. 1992.

[97] D. B. Turner, K. E. Wilk, P. M. G. Curmi, and G. D. Scholes, "Comparison of electronic and vibrational coherence measured by two-dimensional electronic spectroscopy," *The Journal of Physical Chemistry Letters*, vol. 2, pp. 1904–1911, Aug. 2011.

[98] I. A. Heisler, R. Moca, F. V. A. Camargo, and S. R. Meech, "Two-dimensional electronic spectroscopy based on conventional optics and fast dual chopper data acquisition," *Review of Scientific Instruments*, vol. 85, p. 063103, June 2014.

[99] L. A. Bizimana, J. Brazard, W. P. Carbery, T. Gellen, and D. B. Turner, "Resolving molecular vibronic structure using high-sensitivity two-dimensional electronic spectroscopy," *The Journal of Chemical Physics*, vol. 143, p. 164203, Oct. 2015.

[100] B. Spokoyny, C. J. Koh, and E. Harel, "Stable and high-power few cycle supercontinuum for 2d ultrabroadband electronic spectroscopy," *Optics Letters*, vol. 40, pp. 1014–1017, Mar. 2015.

[101] W. Leng and A. M. Kelley, "Resonance Raman intensity analysis of cresyl violet bound to SiO_2 colloidal nanoparticles," *Langmuir*, vol. 19, pp. 7049–7055, Aug. 2003.

[102] G. Lindblad, "On the generators of quantum dynamical semigroups," *Communications in Mathematical Physics*, vol. 48, no. 2, pp. 119–130, 1976.

[103] T. Joo, Y. Jia, J.-Y. Yu, M. J. Lang, and G. R. Fleming, "Third-order nonlinear time domain probes of solvation dynamics," *The Journal of Chemical Physics*, vol. 104, no. 16, p. 6089, 1996.

[104] Y. Nagasawa, A. Watanabe, H. Takikawa, and T. Okada, "Solute dependence of three pulse photon echo peak shift measurements in methanol solution," *The Journal of Physical Chemistry A*, vol. 107, pp. 632–641, Feb. 2003.

[105] L. Bolzonello, A. Polo, A. Volpato, E. Meneghin, M. Cordaro, M. Trapani, M. Fortino, A. Pedone, M. A. Castriciano, and E. Collini, "Two-dimensional electronic spectroscopy reveals dynamics and mechanisms of solvent-driven inertial relaxation in polar BODIPY dyes," *The Journal of Physical Chemistry Letters*, vol. 9, pp. 1079–1085, Mar. 2018.

[106] W. Baumler, A. X. Schmalzl, G. Goss, and A. Penzkofer, "Fluorescence decay studies applying a CW femtosecond dye laser pumped ungated inverse time-correlated single photon counting system," *Measurement Science and Technology*, vol. 3, pp. 384–393, apr 1992.

Acknowledgements

At the end of this thesis I want to take the opportunity to thank all those who supported me in the last years, academically, administratively and personally. Particularly, I want to thank the following people:

- **Prof. Dr. Tobias Brixner** for his contagious enthusiasm for ultrafast spectrocopy in his lectures, for giving me the possibility to do my doctorate in his excellent group and supervising this work, his high scientific standards, his challenging and constructive feedback, and for giving me the opportunity to attend multiple national and international conferences and workshops.
- **Prof. Dr. Patrick Nürnberger**, for his compelling lectures that sparked my interest in laser spectroscopy and chemical dynamics, and for valuable advice in the early stages of the project.
- **Prof. Dr. Ingo Fischer**, for agreeing to be second corrector of this thesis and for turning a blind eye on me being in his social room for table soccer matches with his group members.
- **Dr. Sebastian Röding** for teaching me the day-to-day laboratory work during my Master's thesis, for his guidance concerning spectroscopic theory, and for his ongoing support with pulse-shaper issues.
- **Stefan Müller** for his enthusiasm for multi-dimensional spectroscopy, for working with me on the 2D fluorescence project, for carrying on and unlocking the potential of the setup, and for proof-reading parts of the manuscript.
- **Heiko Hildenbrand**, **Katrin Arnold** and **Johanna Terfrüchte** for working with me on the fluorescence project as intern students and **Niklas Klosterhalfen** during his Bachelor's thesis.
- **Dr. Jakub Dostál**, **Bernhard Huber**, **Christian Kramer** and **Dr. Andreas Steinbacher** for fruitful discussions about nonlinear spectroscopy in general and phase cycling in particular.
- **Dr. Matthias Hensen** for always sharing his profound knowledge, for being a pacifist that would never fire a shotgun, his unique way of pronouncing "jacket", for long heroic nights and for always bringing his friends to their doorsteps.

- **Dr. Andreas Steinbacher** for professional discussions and glorious conferences. The sun shines everywhere in the world, even in Hamburg!
- my first office colleagues **Sebastian Götz**, **Dr. Johannes Knorr** and **Dr. Sebastian Schott** for their constant willingness to help a chemist regarding physical questions.
- **Lysanne Dietrich** and **Lea Ress** for our time in the "girls' office" and for turning a shabby room into a green paradise.
- **Belinda Böhm**, **Sabine Fuchs** and **Sabine Stahl** for their constant willingness to help in all aspects, and especially when the laser decided not to work anymore.
- **Andrea Gehring**, **Susanne Pfarr**, **Anna Rosenfeldt** and **Sandra Stoudek** for their constant reminders to fill in the ERC time sheets and their friendly help in every organizational matter.
- the mechanics and electronic workshop staff **Reiner Eck**, **Wolfgang Liebler**, **Ralf Kohrmann** and **Katharina Schreckling** for the competent solving of all occurring technical issues.
- **Dr. Roland Colditz** and **Dr. Hansi Schmitt** for supervising the PC Praktikum and Hansi also for our *a capella* interpretations of various artists (but mostly Udo!).
- all current and past group members that have not been mentioned here by name, for the cordial atmosphere and professional discussions.
- the **Clariant AG** for supporting me financially throughout my Master's studies with the Deutschlandstipendium.
- my friends outside the working group for reminding me that there is a whole world outside of chemistry and physics, and especially my longstanding flatmate **Sophia**, for her supply of English breakfast in tough times.
- my parents **Eike** and **Michael** for their unlimited support and encouragement in every life situation.
- **Theresa**, for standing by me in troubling times, for your refreshing perspective on life, and for your priceless love.